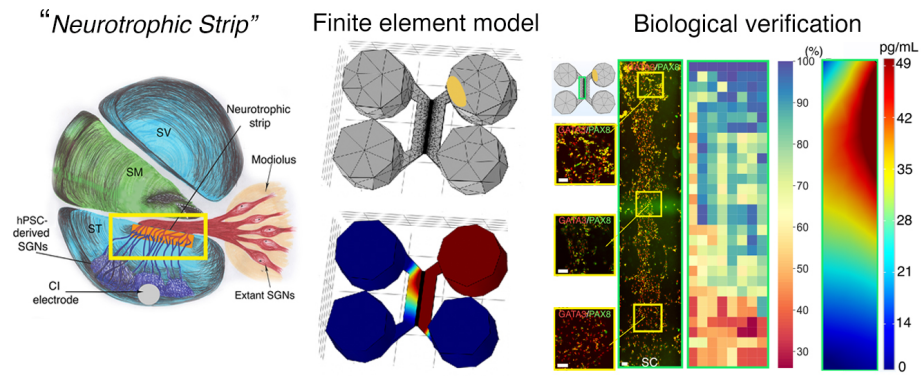


# Graphical Abstract

## Developing the Bioactive Cochlear Implant: Bridging the electrode–neuron gap through neurite guidance

Kevin T. Nella, Benjamin M. Norton, Hsiang-Tsun Chang, Rachel A. Heuer,  
Christian B. Roque, Akihiro J. Matsuoka



# Developing the Bioactive Cochlear Implant: Bridging the electrode–neuron gap through neurite guidance

Kevin T. Nella<sup>a,b</sup>, Benjamin M. Norton<sup>a</sup>, Hsiang-Tsun Chang<sup>a</sup>, Rachel A. Heuer<sup>a</sup>, Christian B. Roque<sup>a</sup>, Akihiro J. Matsuoka<sup>a,c,d,e,\*</sup>

<sup>a</sup>*Department of Otolaryngology–Head and Neck Surgery, Feinberg School of Medicine, Northwestern University, Chicago IL, 60611, USA*

<sup>b</sup>*Department of Mechanical Engineering, Robert R. McCormick School of Engineering and Applied Science, Northwestern University, Evanston IL., 60208, USA*

<sup>c</sup>*Simpson Querrey Institute, Chicago IL, 60611, USA*

<sup>d</sup>*Roxelyn and Richard Pepper Department of Communication Sciences and Disorders, School of Communication, Northwestern University, Evanston, IL., 60201, USA*

<sup>e</sup>*The Hugh Knowles Center for Clinical and Basic Science in Hearing and its Disorders, Evanston, IL. 60201, USA*

---

## Abstract

Although cochlear implant (CI) technology has allowed partial restoration of hearing over the last few decades, persistent challenges remain - including the translation of rich acoustic signals into digital pulse-train signals. Among these challenges, the “electrode-neuron gap” poses the most significant obstacle to advancing past the current plateau in CI performance. Resulting issues include limited performance in noisy environments and sub-optimal ability to decode intonation and music. We propose the development of a “neuroregenerative nexus”—a biological interface that doubly preserves endogenous spiral ganglion neurons (SGNs) while precisely directing the growth of neurites arising from transplanted human pluripotent stem cell (hPSC)-derived otic neuronal progenitors (ONPS) toward endogenous SGNs. We hypothesized that the Polyhedrin Delivery System (PODS®-human brain-derived neurotrophic factor [BDNF])

---

\*Corresponding author: Akihiro J. Matsuoka, Department of Otolaryngology–Head and Neck Surgery, Feinberg School of Medicine, Northwestern University, 676 North St. Clair Street Suite 1325, Chicago, IL 60611, USA. E-mail addresses: amatsuok@nm.org, akihiro.matsuoka@northwestern.edu.

Email addresses: kevinnella2022@u.northwestern.edu (Kevin T. Nella), benjamin.norton@northwestern.edu (Benjamin M. Norton), hsiangtsun.chang@gmail.com (Hsiang-Tsun Chang), racheuer@gmail.com (Rachel A. Heuer), christian.b.roq@gmail.com (Christian B. Roque), amatsuok@nm.org (Akihiro J. Matsuoka)

could stably provide an adequate BDNF concentration gradient to hPSC-derived ONPs and thereby simultaneously facilitate otic neuronal differentiation and directional neurite outgrowth. To test this hypothesis, we first constructed a finite element model to simulate the *in vitro* BDNF concentration gradient generated by PODS®. For biological validation, we conducted *in vitro* cell culture experiments using a multi-chamber microfluidic device, which more closely mirrors the *in vivo* micro-environment of the inner ear than conventional laboratory plates in terms of volume and concentrations of endogenous factors. We were able to generate the optimal BDNF concentration gradient to enable survival, neuronal differentiation toward SGNs, and directed neurite extension of hPSC-derived SGNs. The technique will allow us to further advance our concept of a “neuro-regenerative nexus” by controlling neurite direction of transplanted hPSC-derived ONPs and their endogenous counterparts. This proof-of-concept study provides a step toward the next generation of CI technology.

*Keywords:* human pluripotent stem cells, finite element model, microfluidic device, neurotrophic factor, cochlear implant, neuroelectric interface, stem cell niche, spiral ganglion neurons

*2010 MSC:* 74S05, 62P10, 92C20

---

<sup>1</sup> **1. Introduction**

<sup>2</sup> The cochlear implant (CI), which provides functional restoration in patients  
<sup>3</sup> with sensorineural hearing loss, forms a neuro-electronic interface with the audi-  
<sup>4</sup> tory nervous system [1]. CI technology functions by electrically stimulating the  
<sup>5</sup> extant population of auditory neurons (i.e., spiral ganglion neurons [SGNs]). Al-  
<sup>6</sup> though CI technology has allowed partial restoration of hearing for this patient  
<sup>7</sup> population over the last few decades, persistent challenges remain, including  
<sup>8</sup> the translation of rich acoustic signals into digital pulse-train signals. Central  
<sup>9</sup> to many of these challenges, the “electrode-neuron gap” poses the most signif-  
<sup>10</sup> icant obstacle to advancing past the current plateau in CI performance. This  
<sup>11</sup> phenomenon symptomatically manifests as limited performance in noisy envi-  
<sup>12</sup> ronments and poor ability to decode intonation and music [2], associated with  
<sup>13</sup> a decreased quality of life for many. The gap exists between the CI electrodes  
<sup>14</sup> and the target membranes of dendrites of surviving endogenous SGNs [3]. It  
<sup>15</sup> results in the requirement of larger CI excitation fields, which lead to current  
<sup>16</sup> spread that excites and therefore disables the neighboring electrodes, resulting  
<sup>17</sup> in fewer information channels to the brain [2, 4]. This develops into a vicious  
<sup>18</sup> cycle as fewer information channels to the brain also prompt the need for larger  
<sup>19</sup> CI excitation fields. The width of the gap generally spans hundreds of  $\mu\text{m}$  [5, 6].  
<sup>20</sup> Hahnewald et al. demonstrated *in vitro* that energy needed to elicit a response  
<sup>21</sup> can be reduced by up to 20% by reducing the distance from 40 to zero  $\mu\text{m}$  (early  
<sup>22</sup> postnatal mouse SGN explants were grown on a microelectrode array) [4].

<sup>23</sup> Previous work has introduced the concept of a ”bioactive” CI to resolve the  
<sup>24</sup> electrode-neuron gap *in vivo*[7, 8, 9]. The bioactive CI combines current state-  
<sup>25</sup> of-the-art CI technology with emerging stem cell-replacement therapy in the  
<sup>26</sup> inner ear. In this scheme, transplanted human pluripotent stem cell (hPSC)-  
<sup>27</sup> derived SGNs bridge the gap between the CI and surviving endogenous SGNs.  
<sup>28</sup> However, the issue of establishing synaptic connections between the two cell  
<sup>29</sup> populations remain.

<sup>30</sup> Neurotrophin gradients have been shown to guide hPSC grafts in spinal

31 cord injury [10], direct growth of endogenous SGNs toward CI electrodes in the  
32 scala tympani [11], and enable transplanted hPSC derived otic neuronal pro-  
33 genitors (ONPs) to grow neurites toward the modiolus [9]. Although promising,  
34 these studies failed to observe adequate directed neurite outgrowth (e.g., lack of  
35 synaptic connections between hPSC grafts and endogenous SGNs), presumably  
36 precluding significant improvements in functional recovery of hearing.

37 To confront this issue, we propose the development of a “neuro-regenerative  
38 nexus”—a bioengineered interface that doubly preserves endogenous SGNs and  
39 precisely directs the growth of neurites arising from differentiated transplanted  
40 hPSC-derived ONPs toward the endogenous SGNs. The highlighted yellow-  
41 square area in Figure 1A shows a schematic diagram of this concept. Here, the  
42 neuro-regenerative nexus (shown as an orange rectangle) stimulates directed  
43 neurite outgrowth from both hPSC-derived ONPs and endogenous SGNs via a  
44 neurotrophic factor gradient [12]. While the concept of using a neurotrophin  
45 gradient for directional axonal growth has existed for a few decades, implementa-  
46 tion of neurotrophin gradients has been extremely challenging due to the lack of  
47 self-sustaining neurotrophin delivery methods—their eventual depletion triggers  
48 an accelerated decline in neurite growth and survival of extant SGNs [13, 14, 15].  
49 One major contributor is the biochemical instability of neurotrophins, which suf-  
50 fer from structural fragility and thermo-instability under normal physiological  
51 conditions both *in vitro* and *in vivo*, leading to half-lives typically ranging from  
52 minutes to hours [16]. We set out to mitigate this phenomenon by utilizing the  
53 polyhedrin delivery system (PODS®)—a crystalline growth factor formulation  
54 developed to enable long-term release of growth factors (e.g., neurotrophins)  
55 [17, 18, 19] (Figure 1B). The PODS® technology has adapted viral machinery  
56 to encase a selected growth factor into polyhedrin protein crystals. The resul-  
57 tant growth factor co-crystals have slow degradation profiles under physiological  
58 conditions and, therefore, allow the sustained release of the embedded bioactive  
59 growth factors.

60 We reasoned that a bio-engineered scaffolding integrated with PODS® tech-  
61 nology can establish a neuronal network between transplanted hPSC-derived

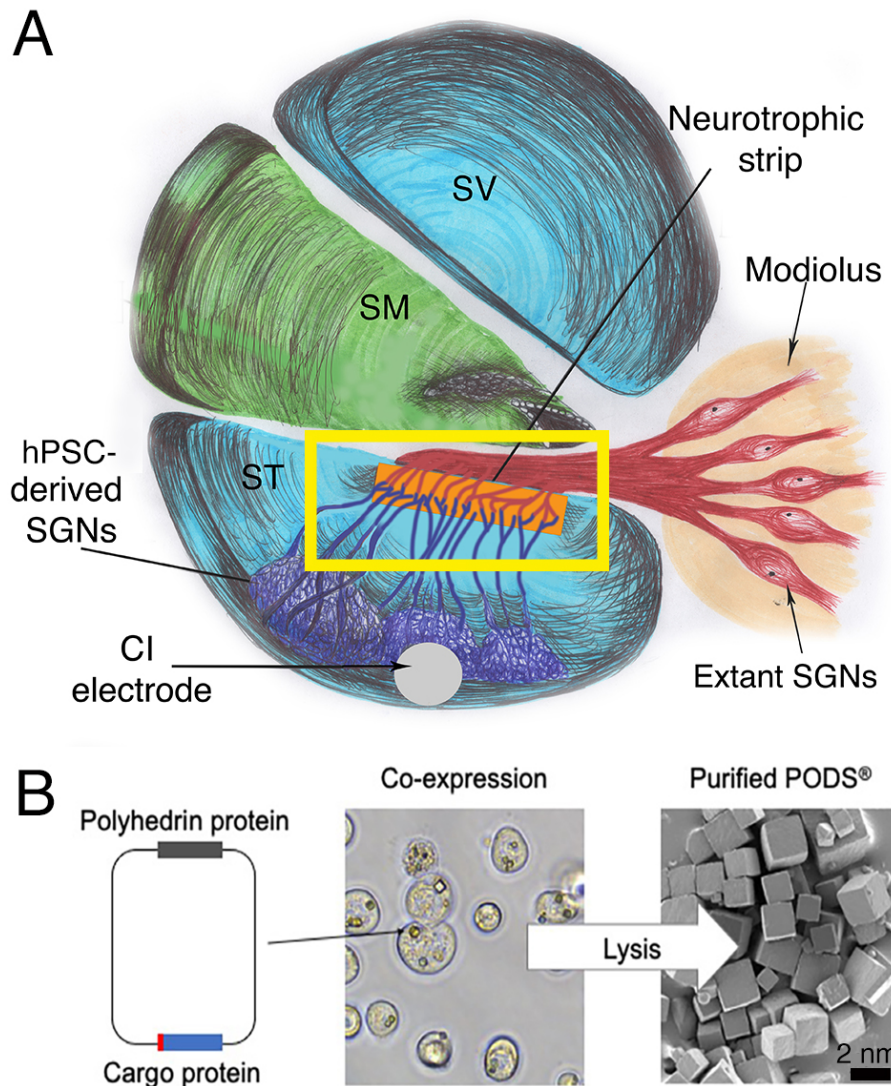


Figure 1: (A): A next-generation bioactive CI and the neuroregenerative nexus. The neural network in this scheme consists of a CI, transplanted stem cell-derived SGNs, a neuroregenerative nexus, and extant/endogenous SGNs (red). Note that neuronal connection is largely absent with hair cells (not shown). (B): Polyhedrin Delivery System (PODS)<sup>®</sup>. PODS<sup>®</sup> crystals are cubic protein co-crystals produced by Sf9 cells (a clonal isolate of *Spodoptera frugiperda* Sf21 cells [IPLB-Sf21-AE], in which the polyhedrin protein and a second “cargo” protein are co-expressed) (Figure 1B, left). Inside the Sf9 cells, polyhedrin proteins self-assemble into cubic crystals (Figure 1B, center) while the active protein, tagged with a short peptide sequence, binds to the growing polyhedrin crystal. The crystals are extracted and purified by simple cell lysis and washes to remove cell debris (Scanning electron micrograph, Figure 1B, right).

62 ONP grafts and extant SGNs in the inner ear. More specifically, we hypothe-  
63 sized that PODS®-recombinant human neurotrophin system could stably pro-  
64 vide and maintain an adequate neurotrophin gradient for the facilitation of  
65 otic neuronal progenitor differentiation and directional neurite outgrowth from  
66 hPSC-derived ONPs. To test this hypothesis, we constructed a finite element  
67 model (FEM) to simulate the *in vitro* neurotrophin concentration gradient gen-  
68 erated by PODS®. In this study, we focus on BDNF—the most studied of  
69 the neurotrophins in the inner ear, and the most vital for functional recovery of  
70 damaged SGNs [20]. For biological validation we employed a multi-chamber mi-  
71 crofluidic device, that which more closely mirrors the *in vivo* micro-environment  
72 of the inner ear than conventional laboratory plates in terms of volume and con-  
73 centrations of endogenous factors [21].

74 **2. Materials and Methods**

75 *2.1. Polyhedrin delivery system*

76 The Polyhedrin Delivery System (PODS®-recombinant human BDNF [rhBDNF])  
77 (Cell Guidance Systems, Cambridge, United Kingdom) was used as the self sus-  
78 taining source of rhBDNF. PODS®-rhBDNF is composed of the polyhedrin  
79 protein formed by *Bombyx mori*, an insect from the moth family *Bombycidae*.  
80 A cargo protein (i.e., rhBDNF) is co-expressed within the polyhedrin crystal  
81 and is slowly released by breakdown of the PODS® crystals via cell-secreted  
82 proteases (Figure 1B)[9, 18, 22].

83 *2.2. Enzyme-linked immunosorbent assay for brain-derived neurotrophic factor*

84 In order to determine the degradation and release kinetics of PODS®-  
85 rhBDNF, an experiment measuring rhBDNF concentrations at sequential time  
86 points was performed. The culture media from both a control and experimental  
87 condition were collected at each time point and immediately stored at -80°C.  
88 An enzyme-linked immunosorbent assay (ELISA) was performed after the final  
89 collection. The same method was applied to measure the degradation kinetics of

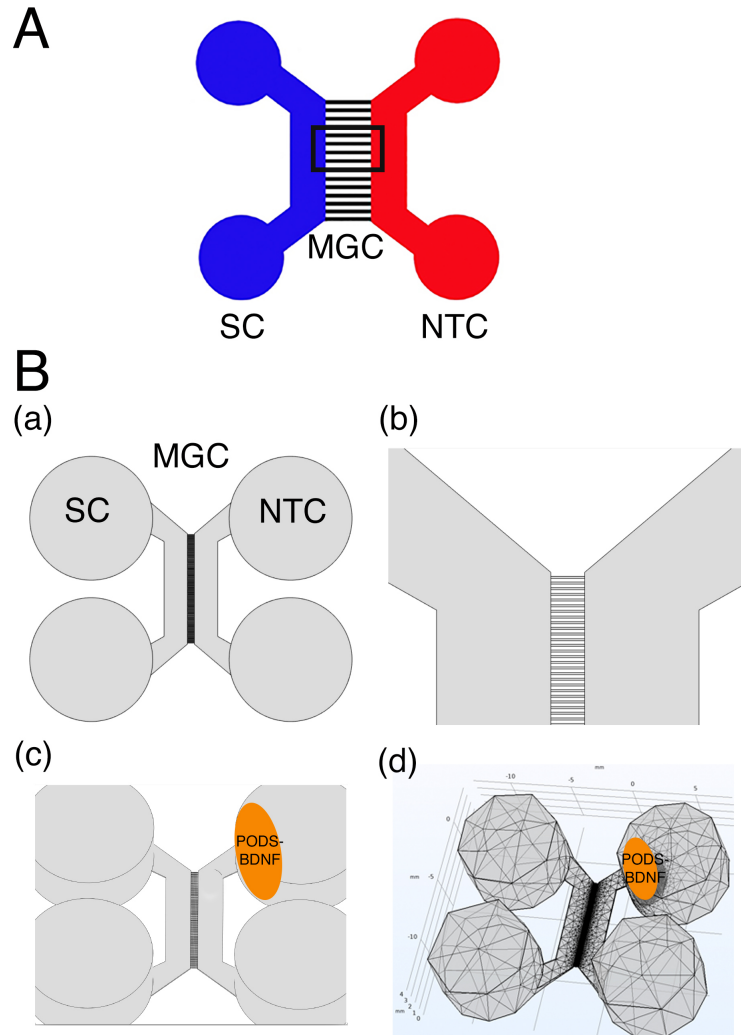


Figure 2: (A): Schematic specification of a Xona™ Microfluidics XC 450. Two main channels (somal compartment (SC) and neurotrophin compartment (NTC)) on either side are connected by a micro-groove channel array (MGC) spanning 450  $\mu\text{m}$ , each channel having a width of 10  $\mu\text{m}$  (black square). The somal compartment contains hPSC-derived late-stage ONPs (shown in black), while the neurotrophin compartment is mainly composed of the secreted factors (i.e., BDNF) that are released from the PODS®-rhBDNF crystals in its upper well. (B):(a) Xona™ Microfluidics XC450 device geometry, created at a 1:1 scale with Autodesk Inventor®, in which the diffusion profile of the released BDNF was modeled. (b) Detail of the microchannels adjoining the two compartments of the Xona™ Microfluidics XC450. (c) Xona™ Microfluidics XC450 device showing the optimal location and geometry of the volume of PODS®-rhBDNF (yellow ellipse). (d): Mesh geometry of the Xona™ XC450 generated with Autodesk Inventor, depicting the localized volume of PODS®-rhBDNF (1  $\mu\text{L}$ ) as an ellipsoid disc.

90 rhBDNF protein with a carrier protein (Bovine Serum Albumin [BSA]) (#248-  
91 BDB-050, R&D Systems, Minneapolis, Minnesota, USA). Experimental conditions  
92 were culture media enriched with 10% fetal bovine serum (FBS) (Thermo  
93 Fisher Scientific, Waltham, MA, USA). All rhBDNF samples were quantified  
94 with a BDNF ELISA kit (# BGK23560; PeproTech, Rocky Hill, New Jersey,  
95 USA), and the results were analyzed with a Synergy HTX Multi-Mode Reader  
96 (BioTek, Winocsiki, Vermont, USA) at a 450 nm wavelength, as instructed by  
97 the manufacturer. Molecular kinetics were then calculated using a self-coded  
98 curve fit analysis as well as the MATLAB Curve Fitting Toolbox (MathWorks,  
99 Natick, CA, USA).

100 *2.3. Sodium dodecyl sulphate–polyacrylamide gel electrophoresis*

101 Sodium dodecyl-sulfate polyacrylamide gel electrophoresis (SDS-PAGE) is  
102 commonly used as a method to separate proteins with molecular masses between  
103 5 and 250 kDa [26], which is suitable for detecting rhBDNF (molecular weight  
104 [MW]: 14kDa [27]) and polyhedrin (MW: ~29 kDa [22]). In this study, SDS-  
105 PAGE was used to formulate the molar ratio of polyhedrin to BDNF. Briefly,  
106 each protein sample was diluted in deionized water and mixed with 6x Laemmli  
107 sample buffer (Bio-Rad Laboratories, Inc., Des Plaines, Illinois [IL], USA) con-  
108 taining 2-mercaptoethanol and heated at 100°C for 5 to 20 minutes. Samples  
109 were then loaded into precast Mini-PROTEAN TGX 4-15% polyacrylamide  
110 mini-gels (Bio-Rad Laboratories, Inc., Des Plaines, IL, USA). Then, 5 mL of  
111 Precision Plus Protein Kaleidoscope Prestained Protein Standards (Bio-Rad  
112 Laboratories, Inc., Des Plaines, IL, USA) were loaded in each gel run. Elec-  
113 trophoresis was performed at room temperature for approximately 90 minutes  
114 using a constant voltage (100V) in 1x solution of Tris-Glycine-SDS electrophore-  
115 sis buffer (Bio-Rad Laboratories, Inc., Des Plaines, IL, USA) until the dye front  
116 reached the end of the 60 mm gel. After electrophoresis, the mini-gels were  
117 rinsed with deionized water 3 times for 5 minutes and were subsequently incu-  
118 bated in SimplyBlue™ SafeStain (ThermoFisher Scientific, Waltham, MA, USA)  
119 for one hour at room temperature with gentle agitation. Images obtained from

120 gels were analyzed using ImageJ 1.53g (December 4, 2020, the National Insti-  
121 tutes of Health, Bethesda, MD, USA [28]). The calculated molar ratio from the  
122 analysis was applied to the COMSOL® Multiphysics model to accurately pre-  
123 dict the rhBDNF concentration gradient arising from PODS®-rhBDNF. SDS-  
124 PAGE was performed according to the manufacturer's technical guide (Bio-Rad  
125 Laboratories, Inc., Des Plaines, IL, USA).

126 *2.4. Western Blot*

127 The identity of the rhBDNF protein detected by SDS-PAGE was confirmed  
128 by Western blot (Bio-Rad Laboratories, Inc., Des Plaines, IL, USA). The polyvinylidene difluoride (PVDF) membrane was prepared in methanol for 30 seconds  
129 before soaking in 1x Tris-Glycine-Methanol transfer buffer for 10 minutes. Wet  
130 transfer was performed at 4°C for approximately 60 minutes using a constant  
131 voltage (100V) in 1X solution of Tris-Glycine-Methanol transfer buffer. After  
132 transfer, the membrane was briefly rinsed with 1X Tris-buffered saline Tween-  
133 20 (TBST) and was subsequently blocked in 5% BSA in TBST for 24 hours  
134 at 4°C with gentle agitation. The membrane was then rinsed with 1x TBST  
135 before incubating with BDNF polyclonal antibody (ThermoFisher Scientific,  
136 Waltham, MA, USA) diluted to 1:1500 in 1% BSA in TBST for 24 hours at  
137 4°C with gentle agitation. Following incubation, the membrane was rinsed in  
138 1x TBST 5 times for 5 minutes to remove unbound primary antibody. Next, the  
139 membrane was incubated in Goat anti-Rabbit IgG (H+L) horseradish peroxidase (HRP) conjugated secondary antibody (ThermoFisher Scientific, Waltham,  
140 MA, USA) diluted to 1:5000 in 1% BSA in TBST for one hour at room tem-  
141 perature with gentle agitation. Following incubation, the membrane was rinsed  
142 in 1x TBST 5 times for 5 minutes to remove unbound secondary antibody. For  
143 sensitive detection, the membrane was treated with Pierce™ ECL Western Blot-  
144 ting Substrate (ThermoFisher Scientific, Waltham, MA, USA), and visualized  
145 using an Azure 600 Digital Imager (Azure Biosystems, Dublin, CA, USA). Elec-  
146 trophoresis buffer for sample condition and run condition was summarized in  
147 Supplementary Table S1.

150      *2.5. Three-dimensional finite element analysis*

151      We used finite element analysis (FEA) to simulate the BDNF concentration  
152      gradient over time in a multi-chamber microfluidic device. FEA is a compu-  
153      tational numerical technique, which approximates mathematical solutions to  
154      partial differential equations (PDEs) that appropriately simulate complex real-  
155      world problems including stress/strain testing, thermal conduction, and diffu-  
156      sion transport in various geometries and materials. In this study, the FEM  
157      allowed us to predict the concentration gradient with respect to time depending  
158      on the quantity of PODS®-rhBDNF introduced into the system. To solve the  
159      FEM, we used COMSOL® Multiphysics (version 5.6 [released on November  
160      11, 2020], COMSOL, Inc., Burlington, Massachusetts [MA], USA), which is a  
161      finite element method solution tool for engineering and scientific research com-  
162      putations. We used sustained-release kinetics for PODS®-rhBDNF determined  
163      from aforementioned ELISA and SDS-PAGE experiments, as well as data from  
164      a previous study by our group [9]. Device geometry was constructed at a 1:1  
165      scale using Autodesk® Inventor 2019.0.2 (Autodesk, Mill Valley, CA, USA)  
166      (Figure 3B). The FEA was computed with a high-performance desktop com-  
167      puter platform equipped with a 64 GB RAM CPU (AMD Ryzen Threadripper  
168      3990X 64-Core, 128-Thread @ 4.3 GHz) and two GPU cards (NVIDIA GeForce  
169      RTX 3080Ti, 12GB 384-bit GFF6X Graphics card).

170      *2.6. Human pluripotent stem cell culture using dual-compartment microfluidic  
171      device*

172      Human embryonic stem cells (hESCs: H7 and H9, passage number 25–35)  
173      were obtained from WiCell Research Institute (Madison, Wisconsin, USA). Hu-  
174      man induced pluripotent stem cells (hiPSCs: TC-1133HKK, passage number  
175      22–35) were generated from human CD34+ cord blood cells using the four  
176      Yamanaka factors at Lonza (Walkersville, Maryland [MD], USA). The hiPSC  
177      cell line (TC-1133HKK) was kindly provided by Healios K.K. (Tokyo, Japan).  
178      hPSC-derived ONPs were derived based on our previously established protocol  
179      (Supplemental Data) [8, 9, 23, 24]. A step-wise series of ligands and growth

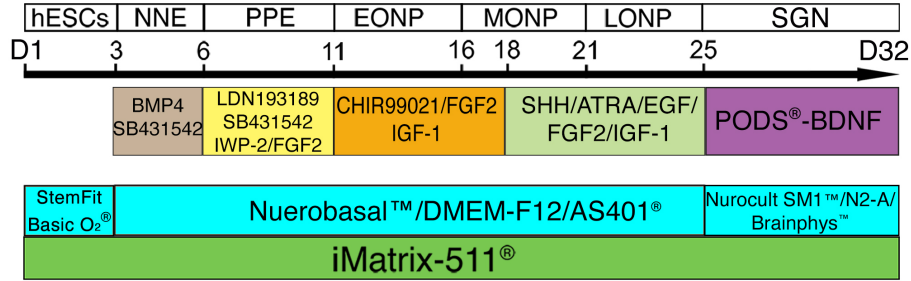


Figure 3: Overview of otic neuronal differentiation protocol for hPSCs. Please see detail in [8, 9, 23, 24] and the Supplemental Data. Each developmental stage is shown at the top, with key treatments shown below. NNE: nonneuronal ectoderm; PPE: preplacodal ectoderm; EONP: early-stage otic neuronal progenitor; MONP: mid-stage otic neuronal progenitor; LONP: late-stage otic neuronal progenitor; BMP4: bone morphogenetic protein 4; SHH: Sonic hedgehog; ATRA: all-trans retinoic acid; EGF: epidermal growth factor; IGF-1: insulin-like growth factor-1; FGF2: fibroblast growth factor 2; N2B27-CDM: chemically defined medium containing N2 and B27 supplements.

180 factors was added to the neuronal induction medium to promote hPSC differen-  
 181 tiation toward the late-stage ONP lineage—the mitotic progenitor population  
 182 that generates SGNs. (Figure 3).

183 Microfluidic devices provided a platform for specifically evaluating axonal  
 184 regeneration [25]. Here, multi-chamber microfluidic devices, Xona™ Microflu-  
 185 idics XC150 and XC450 (Xona™ Microfluidics, Research Triangle Park, North  
 186 Carolina, USA), were used for computational modeling and biological validation  
 187 (Figure 3A–B) of an FEA. The Xona™ device allows for neurites to grow toward  
 188 growth factors in the opposite chamber while limiting migration of derived ONP  
 189 cell bodies due to specific dimensions of the device. The microchannel array be-  
 190 tween the two chambers also mirrors the porous bony separation (osseous spiral  
 191 lamina) between the modiolus (where extant SGNs are localized) and the scala  
 192 tympani (where the biohybrid CI would be implanted).

193 The devices were washed and coated with poly-L-ornithine (PLO, 20 µg/mL  
 194 in H<sub>2</sub>O, Sigma-Aldrich, St. Louis, Missouri [MO], USA) and recombinant  
 195 laminin-511 (iMatrix-511, 0.5 mg/mL, Nacalai USA, San Diego, California [CA],

196 USA) according to the manufacturer-outlined protocol. Next, approximately  
197  $1.75 \times 10^5$  cells (in 20  $\mu\text{L}$  of media) were plated in the somal compartment  
198 through the top and bottom left wells (i.e., total amount of  $3.5 \times 10^5$  hPSC-  
199 derived ONPs were added).

200 A specified quantity of PODS®-rhBDNF was placed in the top right well of  
201 the neurotrophin compartment (Figure 3A–B). hPSC-derived ONPs were cul-  
202 tured for 7 days in the Xona™ device to induce otic neuronal differentiation  
203 and neurite growth. Note that high-density cell cultures were induced to facili-  
204 tate molecular studies as well as the generation of a more biologically relevant  
205 neuronal phenotype (i.e., otic lineage) [25]. Media was topped off daily after  
206 imaging (from 20-40  $\mu\text{L}$  per well). Experiments were done in three biological  
207 replicates unless otherwise specified in Figure captions.

208 *2.7. Immunocytochemistry and image acquisition*

209 On Day 7, 4% (w/v) paraformaldehyde (PFA) (ThermoFisher Scientific,  
210 Waltham, MA, USA) was added to the compartments for 20 minutes to fix the  
211 cells. ICC was used to stain for GATA3, PAX8, and beta-III tubulin. These  
212 three proteins were shown to appropriately characterize ONPs in our previous  
213 studies [8, 9, 24]. Following PBS wash, cultures were blocked with 5% BSA at  
214 room temperature for 1 hour. Cultures were then incubated overnight at 4°C on  
215 a shaker plate in primary antibody solution using Rabbit anti-Beta-III-Tubulin  
216 (1:100, Abcam, Cambridge, MA, USA), Goat anti-PAX8 (1:500, Abcam, Cam-  
217 bridge, MA, USA), and Mouse anti-GATA3 (1:500, R&D Systems, Minneapolis,  
218 MN, USA). Following PBS washes, cultures were incubated at room tempera-  
219 ture for 90 minutes on a shaker plate in secondary antibody solution composed  
220 of Alexafluor647 anti-Rabbit (1:1000, ThermoFisher Scientific, St. Louis, MO,  
221 USA), Alexafluor488 anti-Goat (1:1000, ThermoFisher Scientific, St. Louis,  
222 MO, USA), and Alexafluor594 anti-Mouse (1:1000, ThermoFisher Scientific, St.  
223 Louis, MO, USA) in 1% BSA. Following PBS -/- washes, cultures were incu-  
224 bated with DAPI for 20 minutes (300 nM, ThermoFisher Scientific, St. Louis,  
225 MO, USA). Secondary antibody controls were performed each time multiple

226 primary antibodies were used [29]. Labeling controls (detection controls) were  
227 performed for a sample from each batch of hPSC culture [29]. See Supplemen-  
228 tary Figure S1 for exemplary figures for these control conditions. Results were  
229 imaged using a Nikon Ti2 Widefield Laser Microscope System (Nikon, Tokyo,  
230 Japan). Phase-contrast images were captured on a Nikon Eclipse TE2000-U  
231 inverted microscope (Nikon, Tokyo, Japan). All fluorescence images were ac-  
232 quired on a Zeiss LSM 510 META laser-scanning confocal microscope (Carl  
233 Zeiss, Oberkochen, Germany), a Nikon Ti2 laser laser-scanning confocal micro-  
234 scope (Nikon, Tokyo, Japan), or a Leica SP5 laser-scanning confocal microscope  
235 (Leica, Welzlar, Germany). Observers were blinded to the conditions during  
236 imaging and tracing. In general, the images were processed with a Image J ver.  
237 1.53j or Matlab R2020b. Further detail on image acquisition and quantification  
238 of fluorescent-positive cells can be found in the Supplemental Data.

239 *2.8. Preferred cell orientation analysis*

240 Collective cell migration, where cells organized in a tightly connected fashion  
241 migrate as cohesive structures, is a critical biological process to highlight the  
242 neurotrophin diffusion profile [30]. To evaluate this process, time-lapse acqui-  
243 sition of images of the Xona™ device was performed using an inverted microscope  
244 (Nikon Eclipse TS100, Tokyo, Japan) at Day 1, 3, 5, and 7. Due to the high cell  
245 density required for hPSC-derived late stage ONPs to survive in the somal com-  
246 partment of the Xona™ device, images were not amenable to manual analysis in  
247 most of the cases. To circumvent this problem, we performed a series of image  
248 pre-processings that are mainly based on modified binarization-based extraction  
249 of aliment score methods with some modifications [31]. We used MATLAB Im-  
250 age Processing Toolbox R2020b (version 9.9.0.1495850, September 30th, 2020,  
251 Mathworks, Natick, MA) for analysis. Please see Supplementary Figure S2 for  
252 further detail. The analysis of directional data in general represents a particular  
253 challenge: there is no reason to designate any particular point on the circle as  
254 zero, and it is somewhat arbitrary depending on where one sets a coordinate  
255 [32, 33]. In this study, we used polar coordinates to determine the directionality

256 of preferred cell orientation. For this analysis, we again used MATLAB Image  
257 Processing Toolbox R2020b. See detailed discussion on how we determined the  
258 preferred cell orientation in Supplementary Figure S3.

259 *2.9. Neurite alignment vector assay, neurite growth assay and cell migration*  
260 *assay*

261 The microfluidic device allowed us to culture hPSC-derived ONPs in a po-  
262 larized manner and to directly isolate/analyze neurites. To evaluate the neurite  
263 projection into the neurotrophin compartment by derived otic neurons cultured  
264 in the somal compartment, we performed a neurite alignment vector assay. We  
265 also evaluated the length of neurites that grew from hPSC-derived ONPs. For  
266 these purposes, hPSC-derived ONPs were cultured in a Xona™ XC450 for seven  
267 days and then immunostained with *beta*-III tubulin and DAPI. We used two  
268 ImageJ plug-in toolkits, NeuriteTracer and NeuronJ, to assess neurite align-  
269 ment and neurite growth [34, 35]. Due to the bipolar nature of hPSC-derived  
270 ONPs/SGNs, we measured the two longest neurites from the cells [24, 36].  
271 Please see Supplementary Figure S4 for detailed description of this analysis. We  
272 used hPSC-derived ONPs cultured with 800,000 PODS®-rhBDNF as a positive  
273 control. This quantity was selected based on our FEM in that concentrations  
274 were so high that there was no biologically relevant concentration gradient. As  
275 a negative control, we used 20 ng/mL of recombinant human BDNF (standard  
276 culture condition). To evaluate cell migration across the microgroove channels,  
277 we performed cell migration analysis. We manually counted the number of  
278 ONPs that migrated from the somal compartment into the microchannels and  
279 neurotrophin compartment.

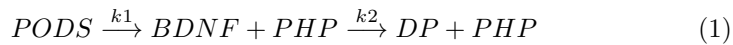
280 *2.10. Statistical analysis*

281 When appropriate, and as indicated in each figure, statistical analysis was  
282 performed. Experimental values are typically expressed as mean and standard  
283 error (SE). The majority of the statistical analyses were performed with Python

3.9.6. (Python Software Foundation, Wilmington, Delaware, USA). The following libraries were used for the statistical analysis: Scipy, Numpy, Matplotlib, and Seaborn [37, 38, 39]. Normal distributions were assumed unless otherwise mentioned.  $P$  values smaller than 0.05 were considered statistically significant. For circular statistics, we derived the sample mean vector and its polar coordinate. Mean and confidence intervals were calculated. We chose confidence coefficient,  $Q$  (e.g.  $Q = 0.95$ ). To analyze the axial nature of data, especially to compute the mean vector angle, we doubled each angle and reduced the multiples modulo  $360^\circ$ . Please see detailed discussion in Supplementary Figure S3 and S5. Rayleigh test of uniformity and V-test were performed to determine whether the samples differ significantly from randomness (i.e., where there is statistical evidence of directionality). One-sample test for the mean angle was performed to test whether the population mean angle is statistically different from the given angle. In all of our circular statistics, von Mises distribution was assumed and also verified. Circular statistics were performed using CircStat: A MATLAB Toolbox [33, 40]. Please see detailed description of circular statistics in Supplementary Figure S3 and S5.

### 3. Results

The appropriate quantity of PODS<sup>®</sup>-rhBDNF crystals to induce an effective neurotrophin gradient for otic neuronal differentiation and directed neurite outgrowth was derived using a three-dimensional FEA that predicts the concentration profile of BDNF formed through the gradual release and diffusion of BDNF from PODS<sup>®</sup>-rhBDNF. First, we quantified the chemical kinetics of this phenomenon with ELISA testing (Figure 4) to establish the parameters for the FEA. Here, two consecutive molecular reactions occur: 1) the breakdown of PODS<sup>®</sup> crystals into polyhedrin protein and rhBDNF, and 2) the degradation of rhBDNF toward the degradation product (Equation (1)).



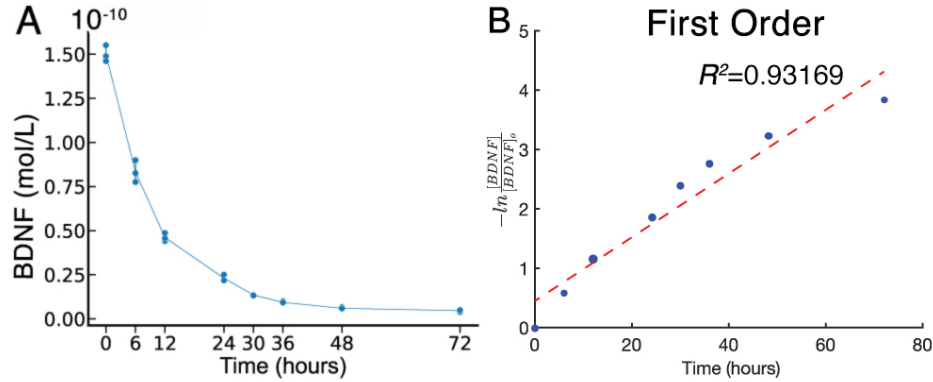


Figure 4: Chemical kinetics of Brain Derived Neurotrophic Factor (BDNF). (A): Concentration of rhBDNF in solution over 72 hours after initial application. (B):  $\frac{1}{[BDNF]}$  data fit to first order curve. Please see other curve fit data in Supplemental Figure 1. Red line: fitted line, blue dots: individual data point.  $k_2$  is defined as slope of fitted curve.

where  $DP$  is the degradation product of the released rhBDNF, PHP is the polyhedrin protein, and  $k_1$  and  $k_2$  are the rate constants ( $\frac{1}{hour}$ ) for their respective reactions.

Degradation kinetics data for rhBDNF was collected while monitoring rhBDNF concentration after introducing a predefined amount into a single well of solution. The data obtained throughout the first 72 hours indicate an exponential decay, suggesting first order kinetics (Figure 4). To confirm this interpretation, we performed a linear and nonlinear least square analysis of the kinetic data with the MATLAB Curve Fitting Toolbox. We found that the corresponding  $R^2$  for the first order curve-fit was 0.93169, confirming that rhBDNF degradation in the experimental condition was indeed first order. The rate constant for a first order reaction is defined to be slope of the plot of the logarithmic ratio between concentration and initial concentration vs time. The value for  $k_2$  is 0.0679 ( $\frac{1}{hour}$ ) (See further detail in Supplementary Figure S7). Furthermore, data for the overarching molecular reaction were collected by similarly monitoring rhBDNF concentration over time after placing a predefined quantity of PODS®-rhBDNF into a single well of solution. The data collected appeared to

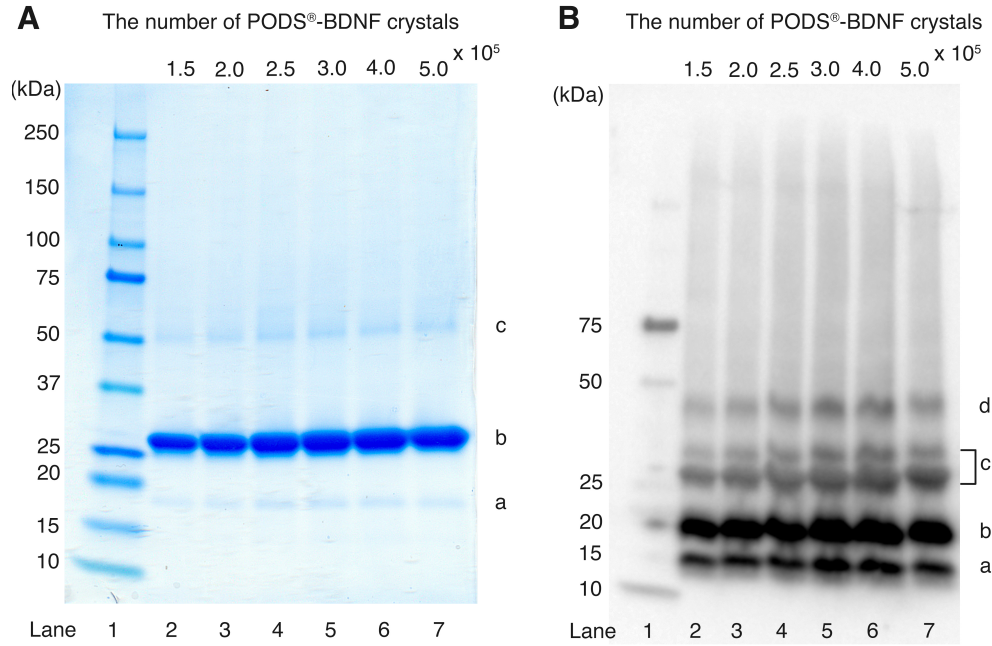


Figure 5: (A): SDS-PAGE analysis of PODS<sup>®</sup>-rhBDNF. Samples containing six quantities of PODS<sup>®</sup>-rhBDNF crystals were run on precast 4-15% polyacrylamide mini-gels and stained with Coomassie G-250 solution for visualization. Protein bands appear at approximately 18.8 (a), 28.0 (b), and 46.8 kDa (c). Lane 1: molecular weight marker. Lanes 2-7: samples containing

<sup>319</sup> fit the general curve for Equation 2, which describes the concentration of the  
<sup>320</sup> intermediate product of two consecutive first order reactions:

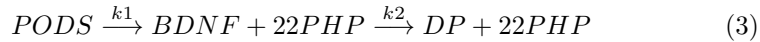
$$C_{rhBDNF} = C_{PODS} \cdot k_1 \cdot \left( \frac{e^{-k_1 \cdot t}}{k_2 - k_1} + \frac{e^{-k_2 \cdot t}}{k_1 - k_2} \right) \quad (2)$$

<sup>321</sup> where  $C_{rhBDNF}$  is the concentration of rhBDNF (the intermediate product)  
<sup>322</sup> and  $C_{PODS}$  is the concentration of PODS<sup>®</sup> [43].

<sup>323</sup> We successfully fit the data to this equation's curve by empirically approxi-  
<sup>324</sup> mating  $k_1$  to be 0.00686 ( $\frac{1}{hour}$ ) after plugging in our calculated  $k_2$  (See further  
<sup>325</sup> detail in Supplementary Figure S7).

<sup>326</sup> SDS-PAGE was used to separate PODS<sup>®</sup>-rhBDNF crystals into its con-  
<sup>327</sup> stituent proteins to determine the molar ratio of polyhedrin to rhBDNF. Vi-

328 sualization with Coomassie G-250 solution (Figure 6A) revealed three distinct  
 329 protein bands at 18.8 (a), 28.0 (b), and 46.8 (c) kDa, which correspond with  
 330 the molecular weights of H1-tagged BDNF monomer, polyhedrin, and H1-tagged  
 331 BDNF monomer conjoined with polyhedrin, respectively. Western blot analy-  
 332 sis was subsequently conducted to confirm the identity of the 18.8 kDa band  
 333 as rhBDNF. Enhanced chemiluminescence (Figure 6B) revealed four protein  
 334 bands at 14.0 (a), 18.8 (b), 37.6 (c), and 46.8 (d) kDa, which correspond  
 335 with the molecular weights of rhBDNF monomer, H1-tagged BDNF monomer,  
 336 H1-tagged BDNF dimer, and H1-tagged BDNF monomer conjoined with poly-  
 337 hedrin. Immunoblot detection of the 18.8 kDa band further implicates its iden-  
 338 tity as rhBDNF. SDS-PAGE images were converted to 8-bit grayscale and mean  
 339 corrected integrated pixel intensity values were calculated for protein bands lo-  
 340 cated at 28.0 and 18.8 kDa; the protein band detected at 46.8 kDa was omitted  
 341 from the final computation. Results indicated that the molecular ratio of poly-  
 342 hedrin to rhBDNF is approximately 22:1 in PODS®-rhBDNF. This transforms  
 343 Equation (1) into:



344 By applying the calculated rate constants with the calculated molar ratio,  
 345 the resulting chemical gradient with respect to time after PODS®-rhBDNF  
 346 placement can be solved for any geometry by applying Fick's second Law of  
 347 diffusion (Equation 4) and the appropriate boundary (Equations 5 and 6) and  
 348 initial conditions (Equation 7):

$$\frac{dC}{dt} = \nabla \cdot (\nabla C \cdot D) - k_2 \cdot C \quad (4)$$

349 Boundary Conditions:

$$\delta C \Big|_{walls} = 0 \quad (5)$$

350 and

$$\delta C \Big|_{PODS} = k_1 \cdot PODS_0 \cdot e^{-k_1 \cdot t} \quad (6)$$

Initial conditions:

$$C \Big|_{t=0} = 0 \quad (7)$$

where  $C$  is the concentration of rhBDNF,  $D$  is diffusivity of rhBDNF (6.76  $\frac{mm^2}{day}$  [44]),  $-k_2 \cdot C$  is the sink term corresponding to the degradation and cell-utilization of the rhBDNF, and  $PODS_0$  is the initial concentration of the cargo protein (i.e., BDNF) within the PODS® crystals. The first boundary condition (Equation 5) declares that the concentration of rhBDNF at the walls of the microfluidic device are fixed at 0. The second boundary condition (Equation 6) represents the exponential nature of the decay of PODS®. Note that both are Neumann boundary conditions.

We empirically tested two commercially available microchannel lengths—(i.e., Xona™ -XC150 [150  $\mu m$ ] and Xona™ -XC450 [450  $\mu m$ ]). This was done first because mass (i.e., BDNF) transport from the neurotrophin compartment through the micro-groove channels into the somal compartment is an important factor in generating the concentration gradient *via* diffusion mixing. We determined that the Xona™ Microfluidics XC450 was more appropriate for this study as the XC-150's micro-groove channels were not long enough to generate and maintain the appropriate concentration gradient throughout the somal compartment as opposed to the XC450. This feature is relevant to human inner ear because the micro-groove channels in the Xona device simulates the pores of the osseous spiral lamina and modiolus between the scala tympani and extant SGNs [41, 42]. Please see Supplementary Figure S6 for detailed measurements of the three-dimensional mesh of the XC450 generated for the FEA.

The finite element analysis was then computed for different PODS®-rhBDNF concentrations and time intervals to empirically optimize the rhBDNF concentration gradient for hPSC-derived ONP differentiation towards SGNs as well as directed neurite extension. Figure 6 shows FEM-computed rhBDNF concentration gradients for 20,000 PODS®-rhBDNF from Day 1–7. Note that the

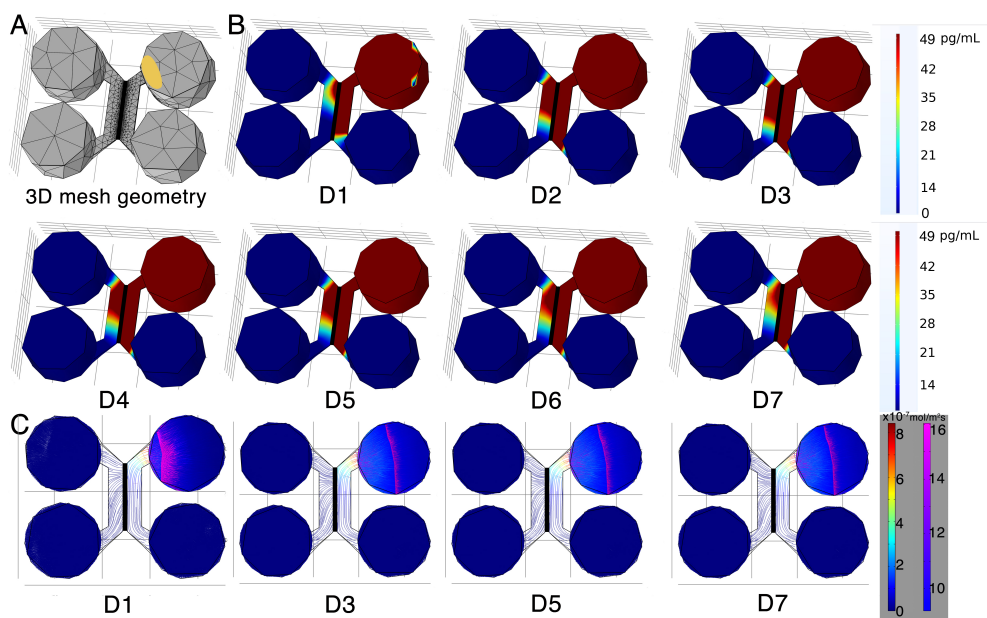


Figure 6: (A): 3D mesh geometry of a Xona™ XC450 created with Autodesk Inventor. A PODS®-rhBDNF ellipsoid disc is shown in yellow. (B): rhBDNF concentration gradient for 20,000 PODS®-rhBDNF from D1–D7. Note that the model does not account for media changes during the culture period. The corresponding color map shown has a range from 0 ng/mL to 49 pg/mL. (C): Diffusion flux ( $\text{mol}/\text{m}^2\text{s}$ ) was computed using COMSOL Chemical Engineering module on D1, D3, D5, and D7.

377 rhBDNF concentrations were greater throughout D2–5 to promote the neuronal  
378 differentiation and neurite outgrowth observed on D7 (Figure 6B). Computed  
379 diffusion flux was uniform throughout D1–7 (Figure 6C). Also note that highest  
380 concentration of rhBDNF released from PODS® crystals was greater than 50  
381 pg/mL, the concentration sufficient for otic neuronal differentiation and neurite  
382 outgrowth of hPSC-derived ONP 3D spheroids determined in our previously  
383 published data [9]. Please see detailed discussion for the empirical optimization  
384 in Supplementary Figure S8.

385 After the biological experiments, we performed quantitative analysis of PAX8  
386 and GATA3 double-positive cells using immunocytochemistry to objectively  
387 compare the degree of otic neuronal differentiation in the hPSC-derived ONPs,.  
388 We chose PAX8 and GATA3 for this analysis because our previous studies in-  
389 dicated high expression of these protein markers in hPSC derived late-stage  
390 ONPs and early-stage hPSC-derived SGNs [8, 9, 24]. Cells were stained in  
391 the somal compartment of the Xona™ device, highlighted in green in Figure  
392 7A. Figure 7B shows the resulting image of cells in the somal compartment,  
393 while a heat-map representation of the percentage of double-positive cells is  
394 shown in Figure 7C. It should be noted that the heat-map is sensitive to the  
395 differences in cell density across channel. This was accounted for by averaging  
396 the double-positivity across three biological replicates. The heat-map indicates  
397 higher double-positivity in the upper region of the somal compartment, which  
398 is closest to the PODS®-rhBDNF disc placement (shown as an orange ellipse  
399 in Figure 7A) in the neurotrophin compartment. Double-positivity decreases as  
400 distance from the PODS®-rhBDNF disc increases, supporting the presence and  
401 effects of a rhBDNF neurotrophin gradient as predicted by our computational  
402 model (Figure 7D).

403 We defined two hypothetical directional angles to predict the orientation of  
404 hPSC-derived ONPs and neurite growth (Figure 8). The  $n$ -dimensional Eu-  
405 clidean space, denoted by  $\mathbb{R}^n$ , is a linear vector space in that we can use polar  
406 coordinates to compute the directionality of cells and neurites [45]. Here, we  
407 used  $n = 1$  and  $2$ . For one-dimensional Euclidean space ( $n = 1$ ), we simply drew

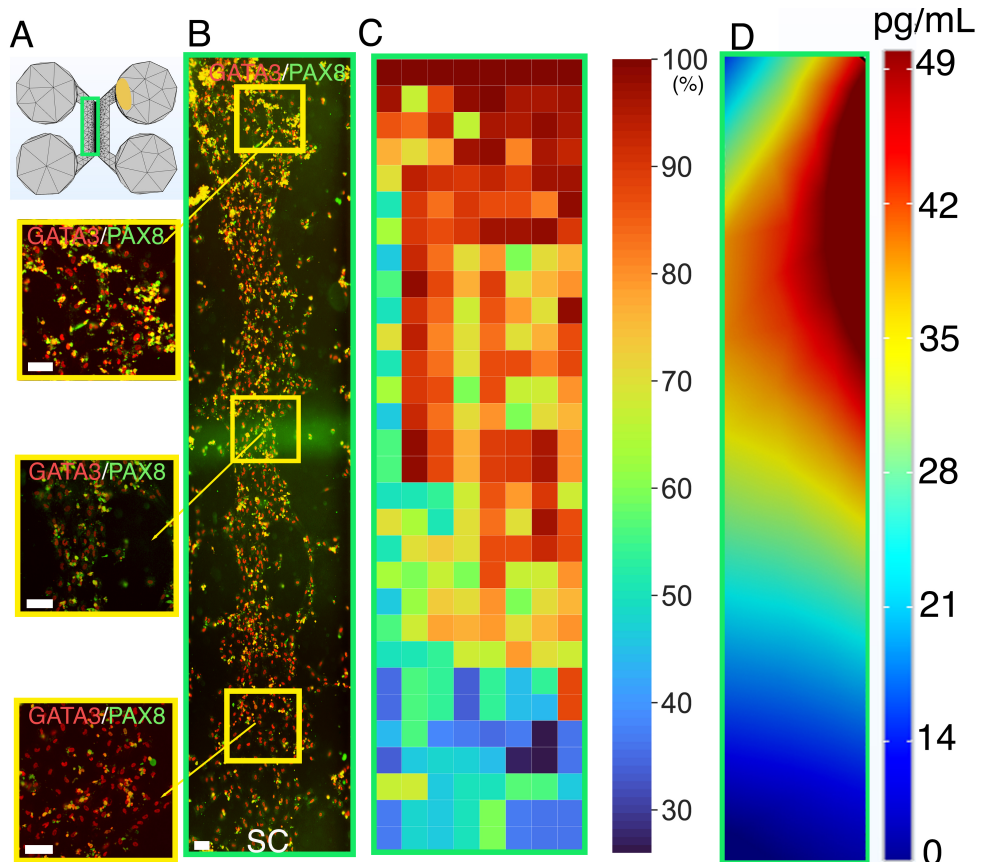


Figure 7: Human PSC-derived late-stage ONPs grown in a microfluidic device at Day 7 were stained for GATA3 (red) and PAX8 (green). (A): Mesh geometry of the microfluidic device Xona™ XC450 constructed with Autodesk Inventor. The green square indicates the cell seeding location in the somal compartment of the device. An ellipsoid PODS®-rhBDNF disc is shown in yellow. (B): Cells were analyzed by staining with neuronal markers GATA3 (red) and PAX8 (green). Yellow highlighted regions are magnified on the left. SC: somal compartment. (C): Heat-map representation of double-positivity of hPSC-derived ONPs in the device for GATA3 and PAX8 ( $n = 3$ ). Double-positivity increases from the lower to the upper portion of the somal compartment, suggesting that the higher BDNF concentration in the upper portion of the device improves differentiation. Scale bar:  $100 \mu\text{m}$ . (D): Prediction of BDNF concentration gradient released from PODS®-rhBDNF at seven days in culture using the finite element model. The corresponding color map is shown with a range from 0–49 pg/mL.

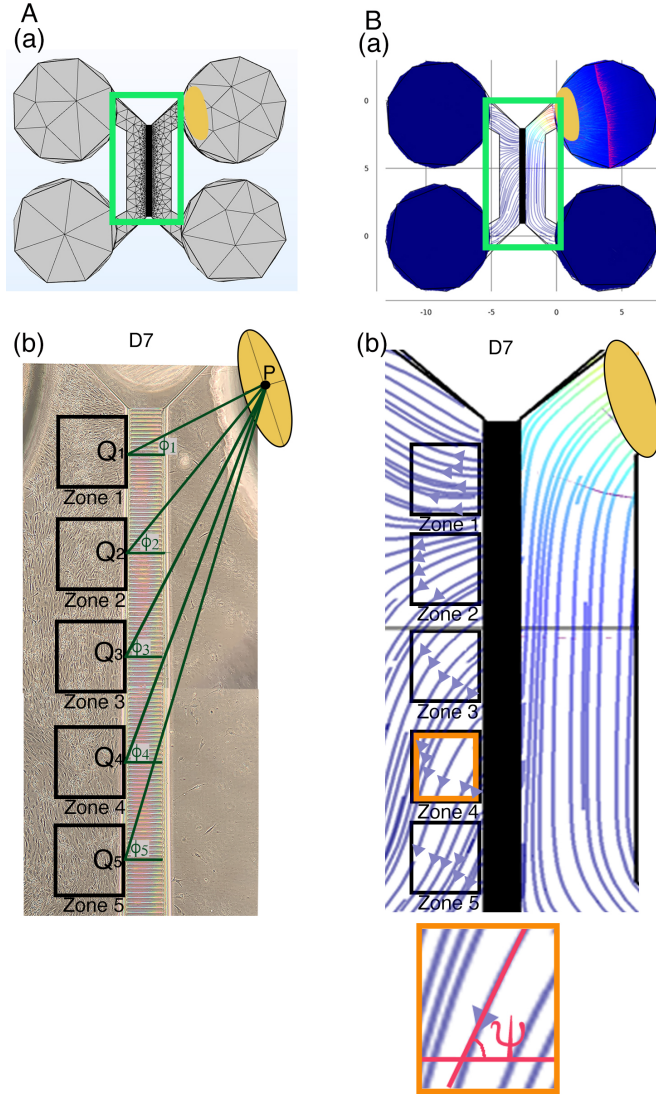


Figure 8: (A): Defining the Euclidean distance angle (EDA). (a) X-Y plane mesh geometry of a Xona™ XC450 device. Green square shows the area corresponding to the phase-contrast image below. An ellipsoid PODS®-rhBDNF disc is shown in yellow. (b) Yellow ellipse indicates the location of a disc containing PODS®-rhBDNF crystals (P: the center of this ellipse). In the somal compartment of the Xona™ XC450 device, we defined Zone 1–5, shown in black squares. A line was drawn from the center of the PODS®-rhBDNF disc (P) to ( $Q_{1-5}$ ) (i.e., the side nearest to microgroove channels) of a pre-designated square (shown as a black square, zone 1–5) [i.e.,zone 1–5]. The Euclidean distance angle (EDA) for zone 1–5 was defined as  $\phi_i$ ,  $i = 1-5$ . (B): Defining diffusion flux angle (DFA). (a) Diffusion flux in the Xona™ XC450. Green squared area shows somal and neurotrophin compartments, which are magnified in (b). (b) Magnified image of diffusion flux in Zones 1–5 in the Xona™ XC450. Orange highlighted zone (zone 4) was magnified at the bottom of (b), defining the DFA ( $\psi$ ).

408 a line for the Euclidean distance—the shortest distance between two points as  
409 shown in Figure 8A(b) (dark green lines). The two points were 1) the center  
410 point of the PODS®-rhBDNF disc ( $P$ ) and 2) the mid point of the medial side  
411 ( $Q_{1-5}$ ) (i.e., the near side to microgroove channels) of a pre-designated square  
412 (shown as a black square, zones 1–5 in Figure 8), respectively. The Euclidean  
413 distance angle (EDA),  $\phi_i$ , was defined as the angle between the horizontal line  
414 zero direction and the line  $PQ_i$  that consists of the Euclidean distance where  $i$   
415 = 1–5.

416

417 For two-dimensional Euclidean space ( $n = 2$ ), we utilized Fick’s first law,  
418 which dictates that the diffusion flux ( $D$ ) is proportional to the concentration  
419 gradient ( $C$ ) [46]. Based on this theorem, the direction of a flow vector can be  
420 used to represent the concentration gradient for directionality. We hypothesized  
421 here that cell orientation is directionally controlled by the flux vector ()driven  
422 by the concentration gradient). Figure 8B shows the flow vectors in the somal  
423 compartment at Day 7 computed by the COMSOL Chemical Reaction Engi-  
424 neering module. We averaged the 10 flow vectors in each of five zones in Figure  
425 8 to compute the diffusion flux angle (DFA),  $\psi_i$ , where  $i = 1–5$  in Figure 8. To  
426 lighten the computational intensity, we reduced the dimension from 3D to 2D  
427 to compute diffusion flux. Please see justification in Supplementary Data. All  
428 of the computed EDAs and DFAs can be found in Supplementary Table 2.

429 Figure 9 shows time-series of microscopic phase-contrast photomicrographs  
430 obtained on Day 1, 3, and 7 in the five zones in the Xona™ XC450. Each  
431 preferred orientation of any given cell was computed and then plotted on a  
432 polar diagram (blue circle). Mean vector angle (MVA, shown in red line on  
433 Figure 9) and median vector angle were computed. All of the polar diagrams  
434 in Figure 9 show that preferred orientation of hPSC-derived ONPs distribute in  
435 an unimodal distribution. We also confirmed that a von Mises distribution is  
436 appropriate for these sets of data (See Supplementary Figure S9). We, therefore,  
437 then tested further to see if the cells had tendency to be oriented to a certain  
438 direction. To test this hypothesis, we used the Rayleigh test of uniformity

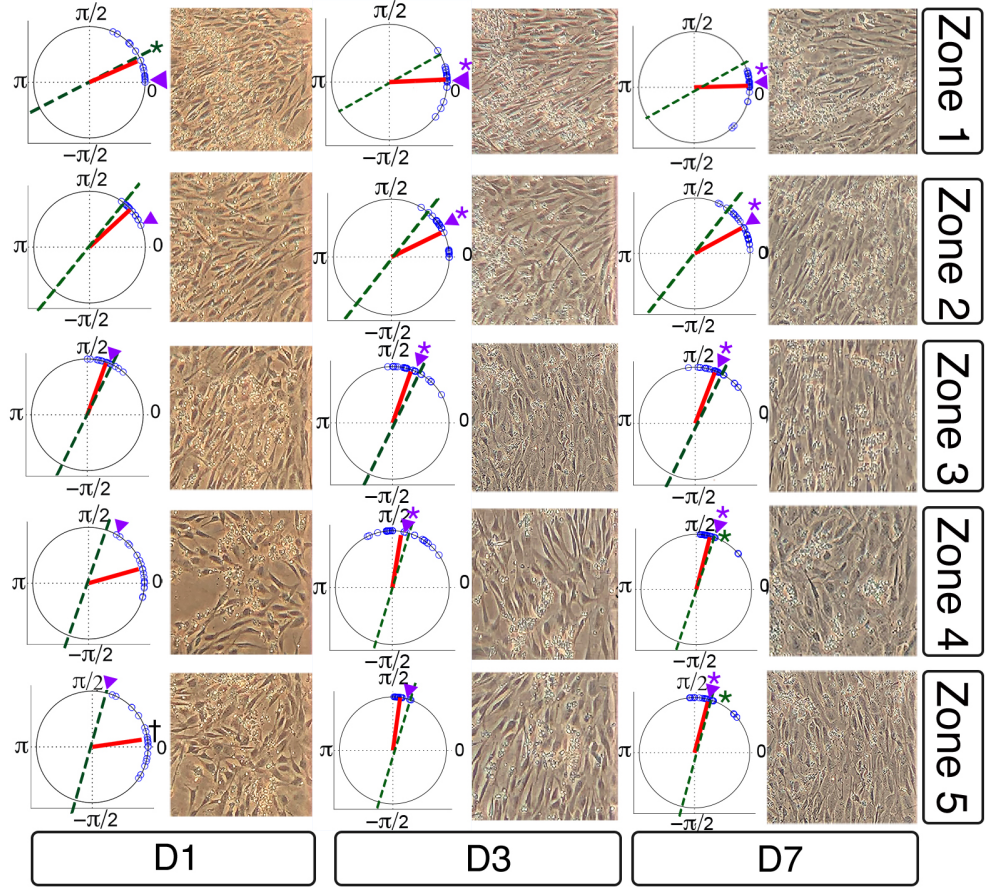


Figure 9: Preferred cell orientation analysis. Sequential phase-contrast images of the somal compartment of the Xona™ XC450 device in zones 1–5 (see Figure 8) on day 1 (D1), day 3 (D3), and day 7 (D7). A corresponding polar histogram indicates preferred orientation of hPSC-derived ONPs as an angle ( $0$ – $2\pi$  radians) in blue circles. Mean vector angle is shown in red line. Green dotted line shows Euclidean Distance Angle (EDA) and purple triangle indicates Diffusion Flow Angle (DFA). † symbol indicates that  $p$  value  $> 0.01$ . \* symbol indicates that the mean vector angle fits within the 95% confidence internal ( $\alpha < 0.05$ .)

439 to evaluate whether there is statistical evidence of circular directionality [32].  
440 Computed  $p$  values for all the 15 conditions were less than 0.05, demonstrating  
441 that all of the conditions had statistically significant directionality. To further  
442 validate whether the observed angles have a tendency to cluster around the two  
443 hypothetical angles (i.e., EDA and DFA), we then performed the V test. Once  
444 again,  $p$  values for all 15 conditions were less than 0.05 except one (Zone 5 on  
445 Day 1), re-demonstrating that most of the conditions had statistically significant  
446 tendencies to cluster around the EDAs and DFAs. Additionally, we performed  
447 one sample test for the mean vector angle, which is similar to a one sample  
448 t-test on a linear scale. There was only one condition (Zone 1, day 1) that was  
449 statistically significant for EDA, whereas most of the conditions on Day 3 and  
450 7 were statistically significant for DFA. Therefore, our results here demonstrated  
451 that hPSC-derived ONPs had greater tendency to cluster around DFA than  
452 EDA. All computed statistical values are shown in Supplementary Table S2.

453 To evaluate the direction of neurites of hPSC-derived ONPs, we first de-  
454 fined EDA in Region 1-3 ( $\phi'_j$ ,  $j = 1 - 3$ ) (Figure 10A) and DFA ( $\psi'_j$ ,  $j = 1-3$ );  
455 similarly defined  $\phi_i$  and  $\psi_i$  as in Figure 8. All of the EDAs and DFAs defined  
456 here can be found in Supplementary Table S3. Polar histograms of the neurite  
457 direction angle in Regions 1–3 indicated that the two longest neurites were bi-  
458 modal in nature (Figure 10B). In contrast, polar histograms of those cultured  
459 with rhBDNF (negative control) and 800,000 PODS<sup>®</sup>-BNDF (positive control)  
460 did not indicate bimodal distribution—the neurites did not show directionality  
461 (Figure 10C). The Rayleigh test of uniformity for both the positive and negative  
462 control were greater than 0.05, demonstrating that both of the conditions had  
463 no statistically significant directionality (Supplementary Table S3: highlighted  
464 in green). We also analyzed the direction of the neurites using circular statistics.  
465 To obtain more realistic mean vector angles, we doubled each angle and reduced  
466 the multiples modulo 360°. In circular statistics, the bimodal distributed data  
467 can be transformed into a unimodal data by doubling the angle [32]. The mean  
468 vector angles in Figure 10D (right column) indicates the situation where the  
469 vectors were canceled out between the two groups of angles distributed in a bi-

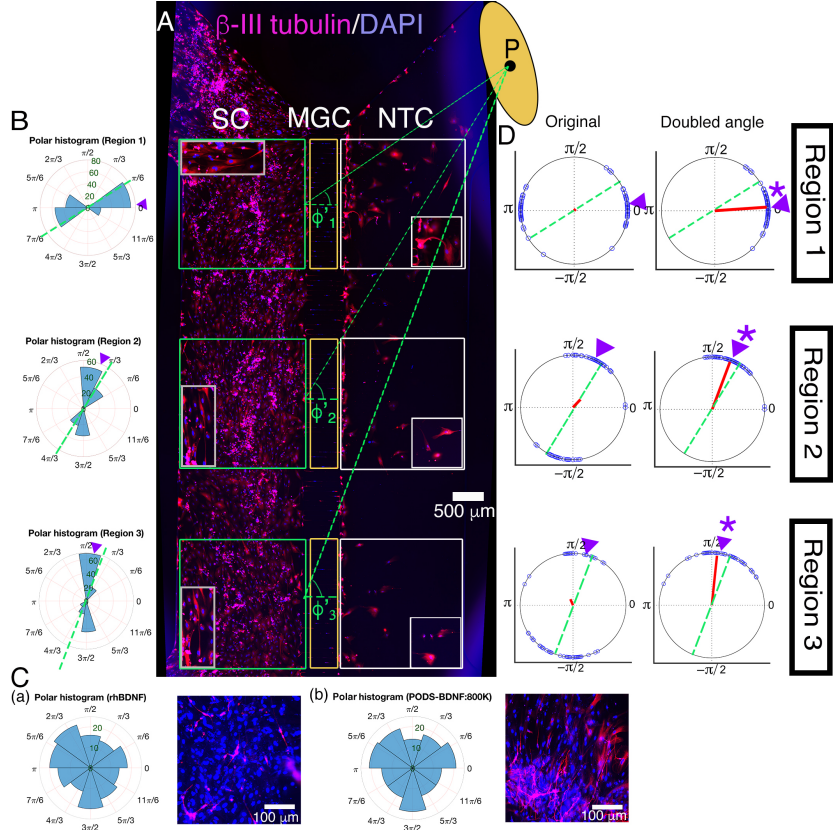


Figure 10: (A): Immunohistochemistry of hPSC-derived ONPs cultured in the Xona™ XC450 for seven days with  $\beta$ -III-Tubulin (pink fluorescence) and DAPI (blue fluorescence). A green line was drawn from the center of the BDNF disc (P) to the mid point of each of three pre-determined squares (Regions 1–3) in the somal compartment to define Euclidean Distance Angle (EDA:  $\phi_i^i$ ,  $i = 1 - 3$ ). Green square: somal compartment (SC); yellow square: microgroove channels (MGC); white square: Neurotrophin compartment (NTC). High-power magnified images of the NTC and SC are shown. An ellipsoid PODS®-rhBDNF disc is shown in yellow. P: the center of the disc.(B): Polar histogram of neurite directional angles of hPSC-derived ONPs in the Xona™ XC450 at Day 7 (D7). The two longest neurites were measured. EDA: green dotted line. DFA: purple triangle. (C): (a) Right: Polar histogram of neurite directional angles of hPSC-derived ONPs cultured with 20 ng/mL of recombinant human BDNF for seven days. Left: Corresponding photomicrograph of immunocytochemistry with  $\beta$ -III tubulin (pink) and DAPI (blue). ()b) Right: Polar histogram of neurite directional angles of hPSC-derived ONPs cultured with 800,000 of PODS®-rhBDNF for seven days. Left: Corresponding photomicrograph of immunocytochemistry with  $\beta$ -III tubulin (pink) and DAPI (blue). (D): A circular plot of neurite directional angle of hPSC-derived ONPs in Region 1–3. Once again, the two longest neurites were plotted on a unit circle. Right column: Original directional angle distribution. Left column: the method of doubling the angle applied to the original data. Each datum point is shown as a blue circle. Mean vector angle is shown as a red line. Green dotted line shows Euclidean Distance Angle (EDA) and purple triangle indicates Diffusion Flow Angle (DFA). \* symbol indicates that the mean vector angle fits within the 95% confidence internal ( $\alpha < 0.05$ .)

470 modal fashion, resulting in inaccurate representation. A circular plot in Figure  
471 10D (right column) showed doubled angles, representing actual representation  
472 of the neurite vector angles. In all of the three regions, the Rayleigh test and V  
473 test for EDA and DFA indicated directionality (Supplementary Table S3). One  
474 sample test for the mean vector angles in Region 1–3 indicated that they were  
475 not statistically different from DFA, but all of the three mean vector angles were  
476 statistically different from EDA.

477 We also stained the devices for  $\beta$ -III tubulin to track neurite growth and  
478 extension across the micro-groove channels as well as cell migration in three  
479 selected regions (Figure 10A). The location of the PODS<sup>®</sup>-rhBDNF disc in  
480 relation to the regions of interest in Figure 11A is indicated by a yellow cir-  
481 cle. Quantitative analyses were performed and summarized in Figure 11B. Our  
482 data indicate that neurite length is dependent on rhBDNF concentration, with  
483 greater amounts of PODS<sup>®</sup>-rhBDNF promoting longer neurite growth (Figure  
484 11B(a)). Lesser amounts of PODS<sup>®</sup>-rhBDNF, however, are necessary to cre-  
485 ate an appropriate concentration gradient. In the presence of 20,000 PODS<sup>®</sup>-  
486 rhBDNF, both neurite extension into the microchannels and cell migration into  
487 the neurotrophin compartment are greatest in the region closest to the BDNF  
488 source and decrease further from the PODS<sup>®</sup>-rhBDNF (Figure 11B(b,c)). Cell  
489 migration is dependent on the distance from the source of BDNF, thus suggest-  
490 ing the presence of a BDNF gradient as predicted by our model.

491 **4. Discussion**

492 *4.1. Challenges of neurotrophin treatment in the inner ear*

493 This proof-of-concept study for the realization of a neuroregenerative nexus  
494 was to ascertain its scientific/technological parameters in a controlled *in vitro*  
495 environment. Neurotrophin gradients have been studied in multiple contexts  
496 [47, 48, 49]. However, it has not been feasible to reliably provide, and maintain,  
497 such a gradient to neurons *in vivo*, primarily because of technical challenges  
498 including failure to provide a reliably sustainable source and practical implan-

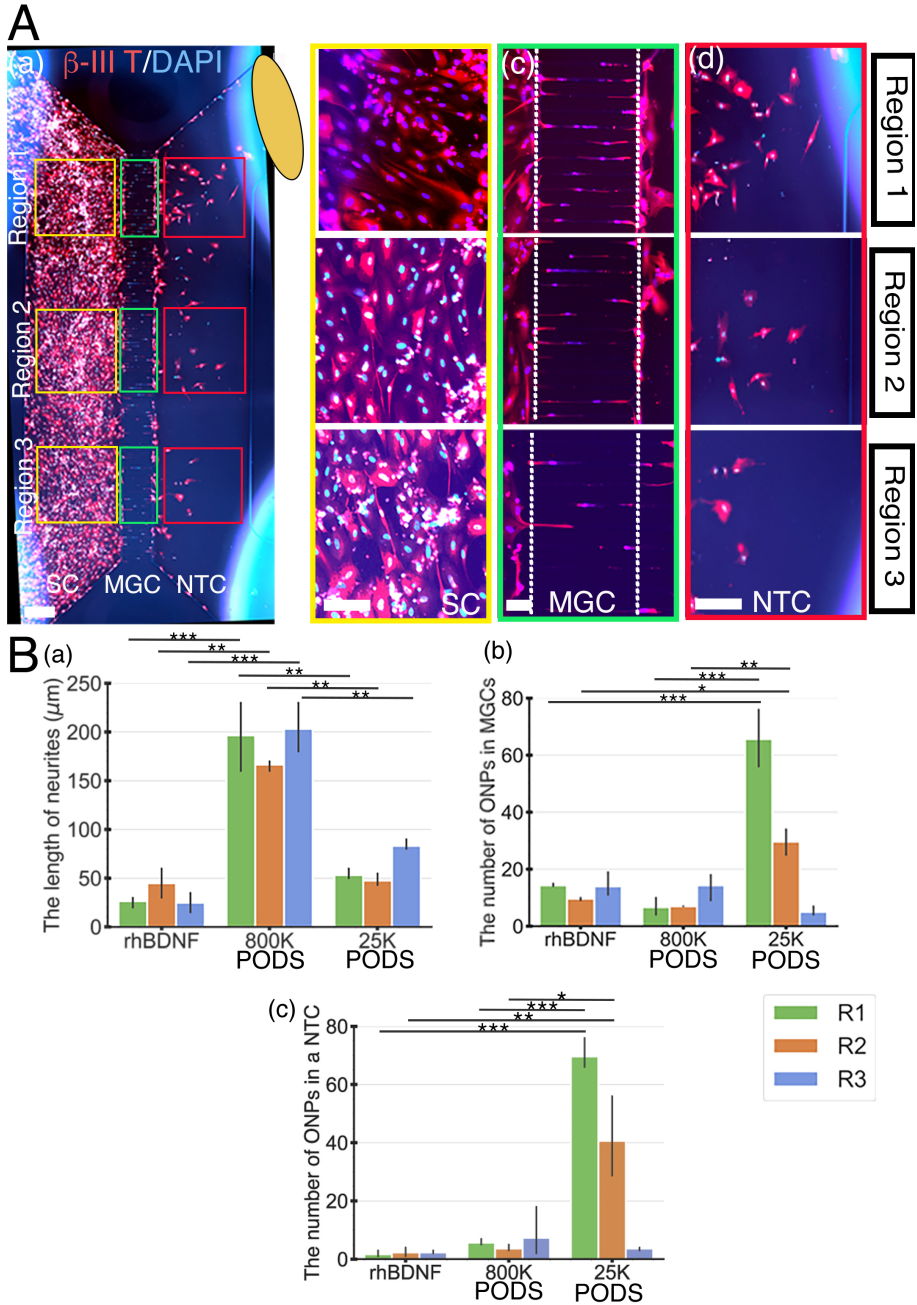


Figure 11: Human PSC-derived late-stage ONPs in the microfluidic device were stained with  $\beta$ -III tubulin (red) and DAPI (blue) to measure cell migration. (A): Late-stage ONPs stained after seven days in culture (a) with regions highlighted and magnified in the somal compartment (b), microgroove channels (c), and neurotrophin compartment (d). SC: somal compartment, MGC: microgroove channels, NTC: neurotrophic compartment. An ellipse-shaped PODS®-rhBDNF disc is shown in yellow. Scale bar (a): 500  $\mu\text{m}$ ; (b)–(d): 100  $\mu\text{m}$ . (B): Quantitative analyses of cell migration and neurite extension in devices using recombinant human BDNF, 800,000 PODS®-rhBDNF, or 20,000 PODS®-rhBDNF. \* :  $p < 0.05$ , \*\*:  $p < 0.01$ , \*\*\*:  $p < 0.001$ .

499 tation. Furthermore, while neurotrophin treatment has been recognized as a  
500 potential treatment for sensorineural hearing loss, there has not been long-term  
501 clinical success in this avenue to date. Most recent relevant clinical trials used  
502 adeno-associated virus (AAV2) to deliver BDNF to the brain [50]. Although  
503 compelling, this treatment does not attempt to precisely control the concentra-  
504 tion of BDNF, which could potentially interfere with normal functions in the  
505 target organ [51]. Furthermore, this treatment may not be applicable to the  
506 inner ear, as the procedure is MR-guided–technically infeasible in the setting of  
507 the inner ear. In this study, we used PODS®-rhBDNF to generate and main-  
508 tain a neurotrophic gradient in a controlled manner. Our results indicate that  
509 20,000 PODS-rhBDNF allowed for a rhBDNF neurotrophin gradient such that  
510 hPSC-derived ONPs survived, differentiated toward human SGNs, and also es-  
511 tablished directional neurite outgrowth in a microfluidic device. Furthermore,  
512 our proposed solution has greater potential to be translated into clinical practice;  
513 in addition to its proven natural self-sustainability, we have shown previously  
514 that implantation of PODS-rhBDNF is met with little immune rejection when  
515 embedded in a nanofibrillar cellulose hydrogel in mice [9].

516 *4.2. Microfluidic device-generated gradient*

517 We utilized a microfluidic device to advance our understanding of direc-  
518 tional neurite growth and otic neuronal differentiation in response to a rhBDNF  
519 concentration gradient [52]. Among many *in vitro* concentration gradient sus-  
520 taining culture devices, microfluidic devices have overcome many of the deficits  
521 that conventional platforms (i.e., the Boyden chamber, Dunn chambers, or com-  
522 partmentalized diffusion chambers) face [52]. Conventional platforms tend to  
523 be sub-optimal in manipulating small volumes of fluid at the order of micro-  
524 liters. Growth factors and proteins can be used in minute amounts in our  
525 microfluidic device, and cultured stem cells are able to interact with endoge-  
526 nous factors at biologically relevant concentrations. As mentioned earlier, this  
527 micro-environment more accurately represents *in vivo* conditions. The Xona™  
528 device can be used to create and sustain a three-dimensional concentration

529 gradient over time (duration and diffusion profile dependent on the chemical  
530 kinetics of the molecule) because of its microchannel array. The device limits  
531 convective flow in the gradient-forming areas by introducing microgroove chan-  
532 nels that generate high fluidic resistance, thereby limiting flow to diffusion. The  
533 high resistance of the microchannel array also prolongs diffusion across them,  
534 thereby increasing gradient formation and decreasing gradient steepness (essen-  
535 tially elongating it). These features motivated us to generate an FEM, which  
536 predicted the rhBDNF gradients resulting from different numbers of PODS®-  
537 BDNF crystals. Note, however, that this environment is geometrically different  
538 from the micro-environment in the inner ear—a mesh geometry of the cochlea will  
539 be needed to compute the PODS®-BDNF crystal number for implementation  
540 in animals, as well as in further clinical translation.

541 *4.3. Brain-derived neurotrophic factor*

542 Over the course of the past 20–30 years, it has been established that BDNF  
543 mediates survival and differentiation activities of SGNs by binding and activat-  
544 ing tyrosine kinase receptor kinase B (TrkB), a member of the larger family of  
545 Trk receptors [20]. Numerous studies have reported that BDNF can palliate  
546 SGN degeneration in ototoxically deafened animals, a widely accepted model  
547 for retrograde trans-synaptic SGN degeneration secondary to hair cell destruc-  
548 tion [13, 14, 53, 54]. Additionally, it has been confirmed that there is a positive  
549 correlation between SGN counts and CI performance [55]. It is then safe to  
550 presume that BDNF application in CI recipients would enhance overall CI per-  
551 formance, by preserving extant SGNs and their neurites. Although promising,  
552 BDNF treatment in humans has not been implemented in the inner ear as simply  
553 introducing BDNF into the inner ear poses significant hurdles.

554 Unsuccessful BDNF treatment is attributed to several factors [56]. The  
555 blood half-life of BDNF protein is extremely short, lasting only 1–10 minutes  
556 in plasma [57, 58] and one hour in CSF [59]. Due to BDNF’s high degrada-  
557 tion rate, simple introduction of BDNF in solution would require continuous  
558 replenishment, impractical in the clinical setting. Furthermore, simply intro-

559 ducing BDNF in solution would presumably promote non-directional neurite  
560 growth where directed neurite growth is essential, especially in the case of our  
561 proposed bioactive CI, due to the lack of a concentration gradient to guide the  
562 growth. Directing neurite growth towards the CI electrode array is pivotal in the  
563 ultimate goal of enhancing performance through the narrowing of the electrode-  
564 neuron gap. The PODS® system provides a gradual release of growth factor  
565 from a localized origin. This steady supply of BDNF from a localized origin not  
566 only generates a concentration gradient, but maintains it over time. As shown  
567 in Figure 6, it is unmistakable that the slow-release nature of PODS®-BDNF  
568 results in a concentration gradient over the course of Day 1–7. As shown in  
569 Figures 7–11, careful calibration of the resulting BDNF gradient can lead to  
570 the promotion of hPSC-derived ONP differentiation towards SGN lineage and  
571 directed neurite extension.

572 It should be noted that our FEM assumes free diffusion of the rhBDNF  
573 protein. In biological cell-culture conditions, rhBDNF released from PODS®-  
574 rhBDNF has tendency to adhere to walls of the culture device, due to its nature  
575 as a "sticky" protein of about 27 kDa (mature BDNF dimer) that is positively  
576 charged under physiological conditions (isoelectric point, pI = 9.4) [60]. As such,  
577 the physio-chemical properties of rhBDNF have rendered the protein prone to  
578 diminished diffusive transport. This phenomenon was observed in preliminary  
579 data where the ONPs failed to survive past 1–3 days of culture (data not shown).  
580 To circumvent this issue we infused the culture media with a carrier protein (i.e.,  
581 BSA), hypothesizing that the albumin would act as a carrier for the released  
582 rhBDNF and allow for free diffusive transport throughout the microfluidic de-  
583 vice [61]. This hypothesis is supported by our sets of biological validation data  
584 (Figures 7–11) clearly showing that hPSC-derived ONPs responded positively  
585 to the modification; they exhibited the expected cell characteristics, body orien-  
586 tation, unidirectional neurite extension, and neurite length. Note that albumin  
587 is the single most highly concentrated protein in the perilymph [62], therefore,  
588 an artificially introduced carrier protein would not be required in future *in vivo*  
589 studies.

590     4.4. *Intracellular signaling initiated by the Tyrosine kinase B receptor*

591     Another issue for consideration in the interpretation of our results is the  
592     intracellular cell-signaling mechanism elicited by rhBDNF. Human BDNF (ma-  
593     ture dimeric form) binds with high affinity to the TrkB receptor. The binding  
594     of BDNF to a TrkB receptor has been proven to be integral to the pro-neuronal  
595     effects of BDNF [20]. Upon binding, TrkB dimerizes and activates intrinsic  
596     kinase activities and other complex sets of intracellular signaling cascades, be-  
597     yond the scope of this study. It should be noted that activation also initiates  
598     internalization by endocytosis and subsequently transports the protein to the  
599     soma [63]. Therefore, the pro-neuronal effects of rhBDNF in our results may be  
600     highly dependent on the status of the TrkB receptors of the cell membrane of  
601     hPSC-derived ONPs. Our previous study has demonstrated strong expression  
602     of the TrkB receptors on derived ONPs [24], however, more detailed studies on  
603     TrkB receptors of hPSC-derived ONPs and SGNs are needed to deepen under-  
604     standing.

605     4.5. *Degradation of PODS® crystals by protease activity*

606     In cell culture, degradation of PODS®-rhBDNF is likely due to the enzy-  
607     matic activity of cell-secreted proteases. The proteases break down the peptide  
608     bonds of the encasing polyhedrin protein, creating openings in the structure to  
609     allow release of the rhBDNF. Therefore, the presence of proteases is impera-  
610     tive for the proper implementation of PODS® technology. These proteases are  
611     additionally responsible for subsequent degradation of the released rhBDNF.  
612     Because cells were not present in the culture media used for the PODS® degra-  
613     dation kinetics experiments, we infused the media with 10% FBS, which in-  
614     herently contains proteases, to promote polyhedrin degradation for rhBDNF  
615     release, and subsequent rhBDNF degradation to acquire parameters that more  
616     accurately describe *in vitro* events. Furthermore, since the cells and PODS  
617     are initially segregated into separate compartments within the culture device,  
618     cell-secreted proteases are unlikely to reach and degrade the PODS in time to  
619     support ONP survival and differentiation, which was apparent in experiments

620 conducted without the addition of FBS (data not shown). Infusion of FBS was  
621 therefore required in these experiments as well. For clinical translation, how-  
622 ever, we presume that cell-secreted proteases will be readily present in the inner  
623 ear and therefore preclude the need for artificial supplementation.

624 *4.6. A concept design: neuroregenerative nexus*

625 The plateau in CI performance in treatment of sensorineural hearing loss has  
626 driven researchers to develop innovative supplementary treatment strategies to  
627 push the field past this hurdle. Our approach strives to directly address the  
628 issue at its core: the electrode-neuron gap—which can lead to serious implica-  
629 tions including low spatial frequency resolution and high power consumption.  
630 The data presented here can be used as a launchpad for the neuroregenerative  
631 nexus (NRN). The proposed NRN is a biointerface concept that integrates a  
632 long-term release source of neurotrophins (i.e., BDNF) with a bioengineered  
633 scaffold to facilitate and maintain a neurotrophic factor gradient. Embedding  
634 the source (e.g., PODS®-rhBDNF) in a biocompatible matrix ensures local-  
635 ization as well as a mechanism to fine-tune degradation and release kinetics.  
636 Implanted in conjunction with the CI, the NRN acts as a supportive bridge  
637 between extant SGNs and transplanted hPSC-derived late stage-ONPs, which  
638 are localized on the implant electrodes themselves (see Figure 1 for schematic).  
639 The NRN would promote survival of both cell populations, differentiation of  
640 the hPSC-derived late stage ONP transplants towards SGNs, directional neu-  
641 rite growth, and synaptogenesis between the two cell populations, effectively  
642 creating a neuronal network between the patient and the CI. As a result, each  
643 electrode would stimulate cell bodies at exceptionally high resolution, essential  
644 for greater tonal differentiability (required for effective social interaction and  
645 music appreciation) and furthermore, increased quality of life for millions. The  
646 successful outcomes presented in this article are pivotal for the realization of a  
647 neuroregenerative nexus that is effective in the *in vivo* environment.

648     *4.7. The limitations of this study and future direction*

649     The reduction of the spacial dimension to 2D for flux analysis certainly af-  
650     fected the flux vector, which determines the predicted concentration vector.  
651     Given that the thickness (i.e., Z-axis) of the microfluidic device was 100  $\mu\text{m}$ ,  
652     we estimated that the effect was minimal. In the future, we plan to use hPSC-  
653     derived 3D spheroids in the somal compartment so that flux vector and concen-  
654     tration gradient vector can more accurately model cell behavior. In this way,  
655     we will be able to circumvent the need to reduce diffusion calculations to 2D for  
656     computation performance in the modeling.

657     We generated an FEM that modeled rhBDNF's biological transport phe-  
658     nomenon from a PODS<sup>®</sup>-rhBDNF disc throughout the Xona<sup>™</sup> device. Note that  
659     in this model, we focused on the major dependent variable, the concentration  
660     and diffusion profile of rhBDNF, to model the biological phenomenon. Other  
661     physical variables that promote cell migration, otic neuronal differentiation, and  
662     neurite growth were not taken into consideration. These variables include elec-  
663     trotaxis (electrical potential), durotaxis (matrix stiffness [i.e., laminin 511 in  
664     our case]) [64], mechanotaxis (cell strain), and lastly cell migration by random  
665     walk [65]. In future studies, we will take these variables into consideration to  
666     more accurately represent the migration and neurite growth of hPSC-derived  
667     ONPs.

668     Insufficient contrast between cells and background in phase contrast images  
669     led to inaccuracies in cell orientation computation for some images. To address  
670     this issue, poor quality images were disregarded in the quantitative analysis.  
671     We occasionally used manual measurement for accuracy. Our future study may  
672     entail automated time-series cell analysis, which would allow more accurate  
673     measurement. Another alternative to address this issue would be with cell  
674     membrane staining in the future.

675     While 20,000 of PODS<sup>®</sup>-rhBDNF were necessary for otic neuronal differen-  
676     tiation and directional neurite outgrowth of hPSC-derived ONPs, this condition  
677     may not be sufficient. For instance, it is still not understood whether the ef-  
678     fects of other neurotrophic factors such as Neurotrophin-3 (NT-3) and Glial cell

line-derived neurotrophic factor could have a positive effect on ONP growth [20, 66, 67]. We plan to investigate the effects of these and other neurotrophic factors in future studies. Other aspects that could impact directional neurite growth include endogenous factors secreted from hPSC-derived ONPs. While our previous study demonstrated that hPSC-derived ONPs only secreted negligible amounts of BDNF, quantified by ELISA [9], we currently lack data on other neurotrophins and molecules that can affect directional neurite growth in the inner ear. Additionally, previous studies have indicated that neurotrophic support of SGNs is mainly composed of BDNF and neurotrophin-3 (NT-3) [20, 60]. Therefore, the potential confounding effects of other neurotrophic factors (i.e, NT-3) and molecules secreted from hPSC-derived SGNs require further investigation.

Despite these limitations, the presented evidence is clear and well grounded –a precisely controlled and maintained BDNF concentration gradient is necessary for directional neurite extension.

## Conclusions

We successfully enabled survival, neuronal differentiation toward SGNs, and directed neurite extension of hPSC-derived ONPs with a neurotrophin gradient. The technique can allow for control of neurite growth of transplanted hPSC-derived ONPs, as well as native, extant SGNs in the inner ear. This proof-of-concept study translates to a step toward next-generation bioactive CI technology.

## Acknowledgment

This work was supported by the American Otological Society Clinician Scientist Award (AJM), the Triological Society/American College of Surgeons Clinician Scientist Award (AJM), the Department of Otolaryngology of Northwestern University (AJM), the NIH (NIDCD) K08 Clinician Scientist Award K08DC13829-02 (AJM), and the Office of the Assistant Secretary of Defense of

707 Health Affairs through the Hearing Restoration Research Program (Award #:  
708 RH170013:WU81XWUH-18-0712). Imaging work was performed at the North-  
709 western University Center for Advanced Microscopy, which is generously sup-  
710 ported by NCI CCSG P30 CA060553 awarded to the Robert H. Lurie Com-  
711 prehensive Cancer Center, for which we thank Peter Duhly, Constadina Ar-  
712 vanitis, Ph.D., David Kirchenbuechler, Ph.D., and Wensheng (Wilson) Liu,  
713 M.D. Some of microfluidic device experiments were performed in the Analytical  
714 bioNanoTechnology (ANTEC) Core Facility of the Simpson Querrey Institute  
715 at Northwestern University, which is supported by the Soft and Hybrid Nan-  
716 otechnology Experimental (SHyNE) Resource (NSFECCS-1542205). We thank  
717 Shreyas Bharadwaj (Cornell University), Kyle Coots (Midwestern University),  
718 Andrew Oleksijew (the University of Nebraska), Duncan Chadly (California In-  
719 stitute of Technology), and Shun Kobayashi (the University of Texas at Austin)  
720 for their contribution to the earlier phases of this project. We thank Sara Dun-  
721 lop (Department of Neurology, Northwestern University), and Dr. Jacqueline  
722 Bond (the University of California San Diego) for assistance in Western Blot  
723 and SDS-PAGE experiments. We also thank Dr. Georgia Minakaki (Depart-  
724 ment of Neurology, Northwestern University) on assistance in ELISA. Finally,  
725 our thanks and appreciation go to our collaborator, Dr. Christian Pernstich  
726 (Cell Guidance Systems), for continuous support and stimulating discussions  
727 on this project since 2015.

728 **References**

- 729 [1] J. G. Naples, M. J. Ruckenstein, Cochlear Implant., Otolaryngologic Clinics  
730 of North America 53 (1) (2020) 87–102. doi:10.1016/j.otc.2019.09.  
731 004.
- 732 [2] B. S. Wilson, M. F. Dorman, Cochlear implants: A remarkable past  
733 and a brilliant future, Hearing Research 242 (1-2) (2008) 3–21. arXiv:  
734 NIHMS150003, doi:10.1016/j.heares.2008.06.005.

- 735 [3] C. Frick, M. Müller, U. Wank, A. Tropitzsch, B. Kramer, P. Senn, H. Rask-  
736 Anderson, K. H. Wiesmüller, H. Löwenheim, Biofunctionalized peptide-  
737 based hydrogels provide permissive scaffolds to attract neurite outgrowth  
738 from spiral ganglion neurons, *Colloids and Surfaces B: Biointerfaces* 149  
739 (2017) 105–114. [doi:10.1016/j.colsurfb.2016.10.003](https://doi.org/10.1016/j.colsurfb.2016.10.003).
- 740 [4] S. Hahnewald, A. Tscherter, E. Marconi, J. Streit, H. R. Widmer, C. Gar-  
741 nham, H. Benav, M. Mueller, H. Löwenheim, M. Roccio, P. Senn, Response  
742 profiles of murine spiral ganglion neurons on multi-electrode arrays., *Jour-*  
743 *nal of neural engineering* 13 (1) (2016) 16011. [doi:10.1088/1741-2560/13/1/016011](https://doi.org/10.1088/1741-2560/13/1/016011).
- 745 [5] R. K. Shepherd, S. Hatsushika, G. M. Clark, Electrical stimulation of  
746 the auditory nerve: The effect of electrode position on neural excitation,  
747 *Hearing Research* 66 (1) (1993) 108–120. [doi:10.1016/0378-5955\(93\)90265-3](https://doi.org/10.1016/0378-5955(93)90265-3).
- 749 [6] M. Tykocinski, L. T. Cohen, B. C. Pyman, T. Roland, C. Treaba, J. Pal-  
750 amara, M. C. Dahm, R. K. Shepherd, J. Xu, R. S. Cowan, N. L. Cohen,  
751 G. M. Clark, Comparison of electrode position in the human cochlea using  
752 various perimodiolar electrode arrays., *The American journal of otology*  
753 21 (2) (2000) 205–211. [doi:10.1016/S0196-0709\(00\)80010-1](https://doi.org/10.1016/S0196-0709(00)80010-1).
- 754 [7] A. Roemer, U. Köhl, O. Majdani, S. Klöß, C. Falk, S. Haumann, T. Lenarz,  
755 A. Kral, A. Warnecke, Biohybrid cochlear implants in human neurosensory  
756 restoration., *Stem cell research and therapy* 7 (1) (2016) 148. [doi:10.1186/s13287-016-0408-y](https://doi.org/10.1186/s13287-016-0408-y).
- 758 [8] R. A. Heuer, K. T. Nella, H. T. Chang, K. S. Coots, A. M. Oleksijew,  
759 C. B. Roque, L. H. Silva, T. L. McGuire, K. Homma, A. J. Matsuoka,  
760 Three-dimensional otic neuronal progenitor spheroids derived from human  
761 embryonic stem cells, *Tissue Engineering - Part A* 27 (3-4) (2021) 256–269.  
762 [doi:10.1089/ten.tea.2020.0078](https://doi.org/10.1089/ten.tea.2020.0078).

- 763 [9] H.-T. Chang, R. A. Heuer, A. M. Oleksijew, K. S. Coots, C. B. Roque, K. T.  
764 Nella, T. L. McGuire, A. J. Matsuoka, An Engineered Three-Dimensional  
765 Stem Cell Niche in the Inner Ear by Applying a Nanofibrillar Cellulose  
766 Hydrogel with a Sustained-Release Neurotrophic Factor Delivery System,  
767 *Acta Biomaterialia* 108 (2020) 111–127. doi:<https://doi.org/10.1016/j.actbio.2020.03.007>.
- 769 [10] L. Taylor, L. Jones, M. H. Tuszynski, A. Blesch, Neurotrophin-3 gradients  
770 established by lentiviral gene delivery promote short-distance axonal bridg-  
771 ing beyond cellular grafts in the injured spinal cord, *Journal of Neuroscience*  
772 26 (38) (2006) 9713–9721. doi:[10.1523/JNEUROSCI.0734-06.2006](https://doi.org/10.1523/JNEUROSCI.0734-06.2006).
- 773 [11] P. Senn, M. Roccio, S. Hahnewald, C. Frick, M. Kwiatkowska, M. Ishikawa,  
774 P. Bako, H. Li, F. Edin, W. Liu, H. Rask-Andersen, I. Pykkö, J. Zou,  
775 M. Mannerström, H. Keppner, A. Homsy, E. Laux, M. Llera, J. P. Lel-  
776 louche, S. Ostrovsky, E. Banin, A. Gedanken, N. Perkas, U. Wank, K. H.  
777 Wiesmüller, P. Mistrik, H. Benav, C. Garnham, C. Jolly, F. Gander, P. Ul-  
778 rich, M. Müller, H. Löwenheim, NANOCI-Nanotechnology Based Cochlear  
779 Implant with Gapless Interface to Auditory Neurons, *Otology and Neuro-*  
780 *urology* 38 (8) (2017) e224—e231. doi:[10.1097/MAO.0000000000001439](https://doi.org/10.1097/MAO.0000000000001439).
- 781 [12] G. J. Goodhill, H. Baier, Axon Guidance: Stretching Gradients to  
782 the Limit, *Neural Computation* 10 (3) (1998) 521–527. doi:[10.1162/089976698300017638](https://doi.org/10.1162/089976698300017638).
- 784 [13] L. N. Gillespie, G. M. Clark, P. F. Bartlett, P. L. Marzella, BDNF-induced  
785 survival of auditory neurons *in vivo*: Cessation of treatment leads to ac-  
786 celerated loss of survival effects, *Journal of Neuroscience Research* 71 (6)  
787 (2003) 785–790. doi:[10.1002/jnr.10542](https://doi.org/10.1002/jnr.10542).
- 788 [14] L. N. Pettingill, R. L. Minter, R. K. Shepherd, Schwann cells geneti-  
789 cally modified to express neurotrophins promote spiral ganglion neuron  
790 survival *in vitro*, *Neuroscience* 152 (3) (2008) 821–828. doi:[10.1016/j.neuroscience.2007.11.057](https://doi.org/10.1016/j.neuroscience.2007.11.057). Schwann.

- 792 [15] R. K. Shepherd, A. Coco, S. B. Epp, Neurotrophins and electrical stim-  
793 ulation for protection and repair of spiral ganglion neurons following  
794 sensorineural hearing loss, Hearing Research 242 (2009) 100–109. doi:  
795 [10.1016/j.heares.2007.12.005](https://doi.org/10.1016/j.heares.2007.12.005).Neurotrophins.
- 796 [16] B. Baseri, J. J. Choi, T. Deffieux, G. Samiotaki, Y. S. Tung, O. Olu-  
797 molade, S. A. Small, B. Morrison, E. E. Konofagou, Activation of sig-  
798 naling pathways following localized delivery of systemically administered  
799 neurotrophic factors across the bloodbrain barrier using focused ultra-  
800 sound and microbubbles, Physics in Medicine and Biology 57 (7). doi:  
801 [10.1088/0031-9155/57/7/N65](https://doi.org/10.1088/0031-9155/57/7/N65).
- 802 [17] K. Ikeda, S. Nagaoka, S. Winkler, K. Kotani, H. Yagi, K. Nakanishi,  
803 S. Miyajima, J. Kobayashi, H. Mori, Molecular Characterization of Bom-  
804 byx mori Cytoplasmic Polyhedrosis Virus Genome Segment 4, Journal of  
805 Virology 75 (2) (2001) 988–995. doi:[10.1128/jvi.75.2.988-995.2001](https://doi.org/10.1128/jvi.75.2.988-995.2001).
- 806 [18] T. Suzuki, T. Kanaya, H. Okazaki, K. Ogawa, A. Usami, H. Watanabe,  
807 K. Kadono-Okuda, M. Yamakawa, H. Sato, H. Mori, S. Takahashi, K. Oda,  
808 Efficient protein production using a Bombyx mori nuclear polyhedrosis  
809 virus lacking the cysteine proteinase gene, Journal of General Virology  
810 78 (12) (1997) 3073–3080. doi:[10.1099/0022-1317-78-12-3073](https://doi.org/10.1099/0022-1317-78-12-3073).
- 811 [19] H. Mori, R. Ito, H. Nakazawa, M. Sumida, F. Matsubara, Y. Minobe,  
812 Expression of Bombyx mori cytoplasmic polyhedrosis virus polyhedrin in  
813 insect cells by using a baculovirus expression vector, and its assembly into  
814 polyhedra, Journal of General Virology 74 (1) (1993) 99–102. doi:[10.1099/0022-1317-74-1-99](https://doi.org/10.1099/0022-1317-74-1-99).
- 816 [20] S. H. Green, E. Bailey, Q. Wang, R. L. Davis, The Trk A, B, C's of  
817 Neurotrophins in the Cochlea., Anatomical record (Hoboken, N.J. : 2007)  
818 295 (11) (2012) 1877–1895. doi:[10.1002/ar.22587](https://doi.org/10.1002/ar.22587).
- 819 [21] I. Meyvantsson, D. J. Beebe, Cell culture models in microfluidic systems,

- 820        Annual Review of Analytical Chemistry 1 (1) (2008) 423–449. doi:10.  
821        1146/annurev.anchem.1.031207.113042.
- 822        [22] Z.-J. Guo, M.-H. Yu, X.-Y. Dong, W.-L. Wang, T. Tian, X.-Y. Yu, X.-D.  
823        Tang, Protein composition analysis of polyhedra matrix of *Bombyx mori*  
824        nucleopolyhedrovirus (BmNPV) showed powerful capacity of polyhedra to  
825        encapsulate foreign proteins., *Scientific reports* 7 (1) (2017) 8768. doi:  
826        10.1038/s41598-017-08987-8.
- 827        [23] A. J. Matsuoka, Z. A. Sayed, N. Stephanopoulos, E. J. Berns, A. R. Wad-  
828        hwani, Z. D. Morrissey, D. M. Chadly, S. Kobayashi, A. N. Edelbrock,  
829        T. Mashimo, C. A. Miller, T. L. McGuire, S. I. Stupp, J. A. Kessler,  
830        Creating a stem cell niche in the inner ear using self-assembling peptide  
831        amphiphiles., *Plos One* 12 (12) (2017) e0190150. doi:10.1371/journal.  
832        pone.0190150.
- 833        [24] A. J. Matsuoka, Z. D. Morrissey, C. Zhang, K. Homma, A. Belmadani,  
834        C. A. Miller, D. M. Chadly, S. Kobayashi, A. N. Edelbrock, M. Tanaka-  
835        Matakatsu, D. S. Whitlon, L. Lyass, T. L. McGuire, S. I. Stupp, J. A.  
836        Kessler, Directed Differentiation of Human Embryonic Stem Cells Toward  
837        Placode-Derived Spiral Ganglion-Like Sensory Neurons, *Stem Cells Trans-  
838        lational Medicine* 6 (2017) 923–936. doi:10.1002/sctm.16-0032.
- 839        [25] H. Al-Ali, S. R. Beckerman, J. L. Bixby, V. P. Lemmon, In vitro models  
840        of axon regeneration, *Experimental Neurology* 287 (Pt 3) (2017) 423–434.  
841        doi:10.1016/j.expneurol.2016.01.020.
- 842        [26] U. K. Laemmli, Cleavage of structural proteins during the assembly of  
843        the head of bacteriophage T4., *Nature* 227 (5259) (1970) 680–685. doi:  
844        10.1038/227680a0.
- 845        [27] A. L. Mandel, H. Ozdener, V. Utermohlen, Identification of pro- and mature  
846        brain-derived neurotrophic factor in human saliva., *Archives of oral biology*  
847        54 (7) (2009) 689–695. doi:10.1016/j.archoralbio.2009.04.005.

- 848 [28] C. A. Schneider, W. S. Rasband, K. W. Eliceiri, NIH Image to ImageJ:  
849 25 years of image analysis, *Nature Methods* 9 (7) (2012) 671–675. [arXiv: arXiv:1011.1669v3](#), [doi:10.1038/nmeth.2089](#).
- 851 [29] R. W. Burry, Controls for immunocytochemistry: an update., *The journal*  
852 *of histochemistry and cytochemistry : official journal of the Histochemistry*  
853 *Society* 59 (1) (2011) 6–12. [doi:10.1369/jhc.2010.956920](#).
- 854 [30] M. B. Mazalan, M. A. B. Ramlan, J. H. Shin, T. Ohashi, Effect of geomet-  
855 metric curvature on collective cell migration in tortuous microchannel devices,  
856 *Micromachines* 11 (7) (2020) 1–17. [doi:10.3390/MI11070659](#).
- 857 [31] F. Xu, T. Beyazoglu, E. Hefner, U. A. Gurkan, U. Demirci, Automated  
858 and adaptable quantification of cellular alignment from microscopic images  
859 for tissue engineering applications, *Tissue Engineering - Part C: Methods*  
860 17 (6) (2011) 641–649. [doi:10.1089/ten.tec.2011.0038](#).
- 861 [32] E. Batschelet, *Circular Statistics in Biology (Mathmatics in Biology Series)*,  
862 1st Edition, Academic Press, New York, NY, 1981.
- 863 [33] P. Berens, M. J. Velasco, CircStat for Matlab: Toolbox for circular statistics  
864 with Matlab, Max–Planck–Institut f ur biologische Kybernetik, Technical  
865 Report No. 184 31 (10) (2009) 1–21. [doi:doi:10.18637/jss.v031.i10](#).
- 866 [34] M. Pool, J. Thiemann, A. Bar-Or, A. E. Fournier, NeuriteTracer: A novel  
867 ImageJ plugin for automated quantification of neurite outgrowth, *Jour-*  
868 *nal of Neuroscience Methods* 168 (1) (2008) 134–139. [doi:10.1016/j.jneumeth.2007.08.029](#).
- 870 [35] E. Meijering, M. Jacob, J.-C. F. Sarria, P. Steiner, H. Hirling, M. Unser,  
871 Design and validation of a tool for neurite tracing and analysis in fluo-  
872 rescence microscopy images., *Cytometry. Part A : the journal of the In-*  
873 *ternational Society for Analytical Cytology* 58 (2) (2004) 167–176. [doi:](#)  
874 [10.1002/cyto.a.20022](#).

- 875 [36] M. Anniko, W. Arnold, T. Stigbrand, A. Strom, The Human Spiral Gan-  
876 glion, ORL 57 (1995) 68–77.
- 877 [37] S. van der Walt, S. C. Colbert, G. Varoquaux, The NumPy Array: A  
878 Structure for Efficient Numerical Computation, Computing in Science En-  
879 gineering 13 (2) (2011) 22–30. doi:10.1109/MCSE.2011.37.
- 880 [38] J. D. Hunter, Matplotlib: A 2D Graphics Environment, Computing in  
881 Science Engineering 9 (3) (2007) 90–95. doi:10.1109/MCSE.2007.55.
- 882 [39] P. Virtanen, R. Gommers, T. E. Oliphant, M. Haberland, T. Reddy,  
883 D. Cournapeau, E. Burovski, P. Peterson, W. Weckesser, J. Bright, S. J.  
884 van der Walt, M. Brett, J. Wilson, K. J. Millman, N. Mayorov, A. R. J.  
885 Nelson, E. Jones, R. Kern, E. Larson, C. J. Carey, I. Polat, Y. Feng,  
886 E. W. Moore, J. VanderPlas, D. Laxalde, J. Perktold, R. Cimrman, I. Hen-  
887 riksen, E. A. Quintero, C. R. Harris, A. M. Archibald, A. H. Ribeiro,  
888 F. Pedregosa, P. van Mulbregt, SciPy 1.0: fundamental algorithms for  
889 scientific computing in Python., Nature methods 17 (3) (2020) 261–272.  
890 doi:10.1038/s41592-019-0686-2.
- 891 [40] P. Berens, CircStat : A MATLAB Toolbox for Circular Statistics , Journal  
892 of Statistical Software 31 (10). doi:10.18637/jss.v031.i10.
- 893 [41] M. Tuncel, H. S. Sürütü, K. M. Erbil, A. Konan, Formation of the cochlear  
894 nerve in the modiolus of the guinea pig and human cochleae., Archives of  
895 medical research 36 (5) (2005) 436–40. doi:10.1016/j.arcmed.2005.02.  
896 003.
- 897 [42] B. Küçük, K. Abe, T. Ushiki, Y. Inuyama, S. Fukuda, Kazuo Ishikawa,  
898 Microstructures of the Bony Modiolus in the Human Cochlea : A Scanning  
899 Electron Microscopic Study, Journal of Electron Microsc 40 (40) (1991)  
900 193–197.
- 901 [43] O. Levenspiel, Chemical Reaction Engineering, 3rd Edition, John Wiley  
902 and Sons, Inc., New York, NY, 1999.

- 903 [44] M. Stroh, W. R. Zipfel, R. M. Williams, S. C. Ma, W. W. Webb, W. M.  
904 Saltzman, Multiphoton microscopy guides neurotrophin modification with  
905 poly(ethylene glycol) to enhance interstitial diffusion, *Nature Materials*  
906 3 (7) (2004) 489–494. doi:10.1038/nmat1159.
- 907 [45] S. Axler, *Linear Algebra Done Right*, 3rd Edition, Springer Publishing,  
908 New York, NY, 2015.
- 909 [46] J. Crank, *The mathematics of Diffusion*, 2nd Edition, Oxford University  
910 Press, London, UK, 1979.
- 911 [47] K. M. Keefe, I. S. Sheikh, G. M. Smith, Targeting Neurotrophins to Specific  
912 Populations of Neurons: NGF, BDNF, and NT-3 and Their Relevance  
913 for Treatment of Spinal Cord Injury., *International journal of molecular*  
914 *sciences* 18 (3). doi:10.3390/ijms18030548.
- 915 [48] B. I. Awad, M. A. Carmody, M. P. Steinmetz, Potential role of growth  
916 factors in the management of spinal cord injury., *World Neurosurgery* 83 (1)  
917 (2015) 120–131. doi:10.1016/j.wneu.2013.01.042.
- 918 [49] E. R. n. Hollis, M. H. Tuszynski, Neurotrophins: potential therapeutic tools  
919 for the treatment of spinal cord injury., *Neurotherapeutics : the journal of*  
920 *the American Society for Experimental NeuroTherapeutics* 8 (4) (2011)  
921 694–703. doi:10.1007/s13311-011-0074-9.
- 922 [50] A. H. Nagahara, B. R. Wilson, I. Ivasyk, I. Kovacs, S. Rawalji, J. R.  
923 Bringas, P. J. Piviroto, W. S. Sebastian, L. Samaranch, K. S. Bankiewicz,  
924 M. H. Tuszynski, MR-guided delivery of AAV2-BDNF into the entorhi-  
925 nal cortex of non-human primates., *Gene therapy* 25 (2) (2018) 104–114.  
926 doi:10.1038/s41434-018-0010-2.
- 927 [51] S. D. Croll, C. Suri, D. L. Compton, M. V. Simmons, G. D. Yan-  
928 copoulos, R. M. Lindsay, S. J. Wiegand, J. S. Rudge, H. E. Scharfman,  
929 Brain-derived neurotrophic factor transgenic mice exhibit passive avoid-  
930 ance deficits, increased seizure severity and in vitro hyperexcitability in

- 931       the hippocampus and entorhinal cortex., Neuroscience 93 (4) (1999) 1491–  
932       1506. doi:[10.1016/s0306-4522\(99\)00296-1](https://doi.org/10.1016/s0306-4522(99)00296-1).
- 933       [52] A. Dravid, S. Parittotokkaporn, Z. Aqrawe, S. J. O'Carroll, D. Svirskis,  
934       Determining Neurotrophin Gradients in Vitro to Direct Axonal Outgrowth  
935       following Spinal Cord Injury, ACS Chemical Neuroscience 11 (2) (2020)  
936       121–132. doi:[10.1021/acscchemneuro.9b00565](https://doi.org/10.1021/acscchemneuro.9b00565).
- 937       [53] T. Yamagata, J. M. Miller, M. Ulfendahl, N. P. Olivius, R. A. Altschuler,  
938       I. Pyykkö, G. Bredberg, Delayed neurotrophic treatment preserves nerve  
939       survival and electrophysiological responsiveness in neomycin-deafened  
940       guinea pigs., Journal of neuroscience research 78 (1) (2004) 75–86. doi:  
941       [10.1002/jnr.20239](https://doi.org/10.1002/jnr.20239).
- 942       [54] M. P. Zanin, M. Hellstr??m, R. K. Shepherd, A. R. Harvey, L. N. Gillespie,  
943       Development of a cell-based treatment for long-term neurotrophin expres-  
944       sion and spiral ganglion neuron survival, Neuroscience 277 (2014) 690–699.  
945       doi:[10.1016/j.neuroscience.2014.07.044](https://doi.org/10.1016/j.neuroscience.2014.07.044).
- 946       [55] M. Seyyedi, L. Viana, J. J. Nadol, Within-subject comparison of word  
947       recognition and spiral ganglion cell count in bilateral cochlear implant  
948       recipients, Otol Neurotol 35 (8) (2014) 1446–1450. doi:[10.1097/MAO.000000000000443](https://doi.org/10.1097/MAO.000000000000443).Within-Subject.
- 949
- 950       [56] A. Henriques, C. Pitzer, A. Schneider, Neurotrophic growth factors for the  
951       treatment of amyotrophic lateral sclerosis: where do we stand?, Frontiers  
952       in neuroscience 4 (2010) 32. doi:[10.3389/fnins.2010.00032](https://doi.org/10.3389/fnins.2010.00032).
- 953       [57] J. F. Poduslo, G. L. Curran, Permeability at the blood-brain and  
954       blood-nerve barriers of the neurotrophic factors: NGF, CNTF, NT-3,  
955       BDNF, Molecular Brain Research 36 (2) (1996) 280–286. doi:[10.1016/0169-328X\(95\)00250-V](https://doi.org/10.1016/0169-328X(95)00250-V).
- 956
- 957       [58] T. Sakane, W. M. Pardridge, Carboxyl-directed pegylation of brain-derived

- 958 neurotrophic factor markedly reduces systemic clearance with minimal loss  
959 of biologic activity (1997). doi:10.1023/A:1012117815460.
- 960 [59] R. G. Soderquist, E. D. Milligan, E. M. Sloane, J. A. Harrison, K. K.  
961 Douvas, J. M. Potter, T. S. Hughes, R. A. Chavez, K. Johnson, L. R.  
962 Watkins, M. J. Mahoney, PEGylation of brain-derived neurotrophic factor  
963 for preserved biological activity and enhanced spinal cord distribution.,  
964 Journal of biomedical materials research. Part A 91 (3) (2009) 719–729.  
965 doi:10.1002/jbm.a.32254.
- 966 [60] M. Sasi, B. Vignoli, M. Canossa, R. Blum, Neurobiology of local and inter-  
967 cellular BDNF signaling, Pflugers Archiv : European journal of physiology  
968 469 (5-6) (2017) 593–610. doi:10.1007/s00424-017-1964-4.
- 969 [61] X. Li, Y. Su, S. Liu, L. Tan, X. Mo, S. Ramakrishna, Encapsulation  
970 of proteins in poly(l-lactide-co-caprolactone) fibers by emulsion electro-  
971 spinning, Colloids and Surfaces B: Biointerfaces 75 (2) (2010) 418–424.  
972 doi:10.1016/j.colsurfb.2009.09.014.
- 973 [62] E. E. L. Swan, M. Peppi, Z. Chen, K. M. Green, J. E. Evans, M. J.  
974 McKenna, M. J. Mescher, S. G. Kujawa, W. F. Sewell, Proteomics analysis  
975 of perilymph and cerebrospinal fluid in mouse., The Laryngoscope 119 (5)  
976 (2009) 953–958. doi:10.1002/lary.20209.
- 977 [63] T. Numakawa, S. Suzuki, E. Kumamaru, N. Adachi, M. Richards,  
978 H. Kunugi, BDNF function and intracellular signaling in neurons, Histology  
979 and Histopathology 25 (2) (2010) 237–258. doi:10.14670/HH-25.237.
- 980 [64] C. Gentile, Engineering of Spheroids for Stem Cell Technology, Cur-  
981 rent Stem Cell Research & Therapy 11 (2016) 652–665. doi:10.2174/  
982 1574888x10666151001114848.
- 983 [65] H. Berg, Random Walks in Biology, Princeton Universti Press, Prinston,  
984 NJ, 1983.

- 985 [66] H. Li, F. Edin, H. Hayashi, O. Gudjonsson, N. Danckwardt-Lillies, H. En-  
986 gqvist, H. Rask-Andersen, W. Xia, Guided growth of auditory neurons:  
987 Bioactive particles towards gapless neural electrode interface, *Biomaterials*  
988 122 (2017) 1–9. doi:10.1016/j.biomaterials.2016.12.020.
- 989 [67] J. Schulze, H. Staeker, D. Wedekind, T. Lenarz, A. Warnecke, Expression  
990 pattern of brain-derived neurotrophic factor and its associated receptors:  
991 Implications for exogenous neurotrophin application., *Hearing Research* 413  
992 (2020) 108098. doi:10.1016/j.heares.2020.108098.